ACS APPLIED ELECTRONIC MATERIALS

pubs.acs.org/acsaelm

Spotlight on Applications

Advancing Solid-State Batteries via Thin-Film Electrolytes Fabricated by Pulsed Laser Deposition

Prince Sharma, Gen Hasegawa, Sihao Xing, and Naoaki Kuwata*

Cite This: *ACS Appl. Electron. Mater.* 2026, 8, 4855−4875

Read Online

ACCESS | Metrics & More | Article Recommendations

ABSTRACT: The growing demand for compact, and reliable energy storage is driving innovation across electric vehicles, grid systems, and miniaturized electronics. The continued miniaturization of devices requires ultrathin and highly reliable energy storage capable of autonomous operation in rigid, flexible, and cryogenic platforms. Thin-film solid-state batteries (TFSSBs) are emerging as a key solution, with thin-film solid electrolytes (SEs) enabling precise control over ionic transport, interfacial stability, and mechanical resilience at reduced dimensions. Fabrication techniques such as pulsed laser deposition (PLD), physical vapor deposition, atomic layer deposition (ALD), and solution-based methods allow nanoscale tuning of electrolyte composition and structure, enhancing ionic conductivity and electrochemical performance. This article highlights the critical role of TFSEs in advancing solid-state batteries (SSBs), emphasizing PLD for its exceptional precision and tunability. By linking deposition parameters to ionic transport and interface dynamics through operando X-ray diffraction, Raman spectroscopy, and time-of-flight secondary ion mass spectrometry, this spotlight article also outlines fabrication principles and research pathways to accelerate the translation of TFSSBs from laboratory prototypes to practical, scalable devices.

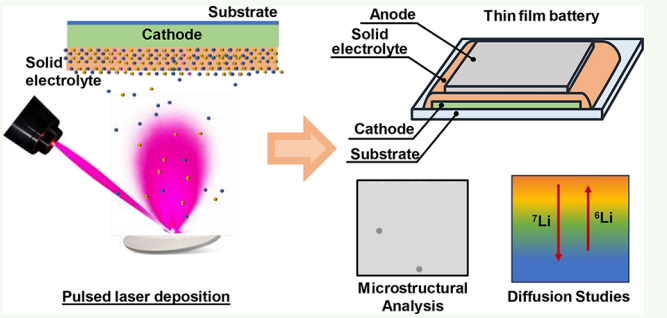

KEYWORDS: *pulsed laser deposition, thin-film solid electrolyte, thin-film solid-state batteries, lithium-ion conductivity, interface engineering, epitaxial thin films, TOF-SMS, ionic transport mechanisms*

INTRODUCTION

The rapid miniaturization of microelectronic, MEMS, photonic, and wearable systems has intensified the demand for compact, reliable, and integrable energy-storage solutions that can operate autonomously within microscale architectures.[1,2] A conventional liquid-electrolyte batteries are fundamentally constrained in such platforms because of their safety risks, leakage, packaging overhead, and incompatibility with semiconductor manufacturing workflows. These limitations become particularly more severe in the case of implantable medical devices, CMOS-based sensors, RFID tags, and distributed IoT nodes. In this kind of system, long-term stability, maintenance-free operation, and direct integration with silicon circuitry are non-negotiable requirements.[3,4] Thin-film solid-state batteries (TFSSBs) have therefore emerged as a critical enabling technology. TFSSBs are constructed from ultrathin solid electrodes and ion-conducting solid electrolyte (SE). They offer intrinsic safety, excellent thermal and chemical stability, and seamless compatibility with wafer-scale microfabrication.[5,6]

Despite their clear technological promise and decades of development, TFSSBs continue to face fundamental materials and processing challenges. Even the industrial benchmark of SE, which is lithium phosphorus oxynitride (LiPON) and related amorphous electrolytes show moderate ionic conductivity, susceptibility to interfacial degradation under high current densities and limited mechanical compliance. It results in restricted power scaling and long-term reliability. While LiPON is best known in bulk form due to their wide electrochemical stability window and favorable interfacial behavior with Li metal and oxide cathodes.[7,8] However, it still lacks in thin-film form. Apart from LiPON, many other high-conductivity bulk SEs such as sulfides and complex oxides are also proven to be difficult to translate into ultrathin, dense, and chemically stable films due to volatility, reactivity, and phase instability during deposition.[9−11] All these issues further compounded by the strong dependence of defect chemistry, ionic transport, and interphase formation during deposition processes. Most importantly, the deposition methods, such as pulsed laser deposition (PLD), RF sputtering, atomic layer deposition

Received: January 29, 2026
Revised: May 18, 2026
Accepted: May 18, 2026
Published: June 8, 2026

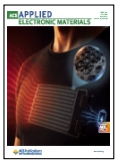

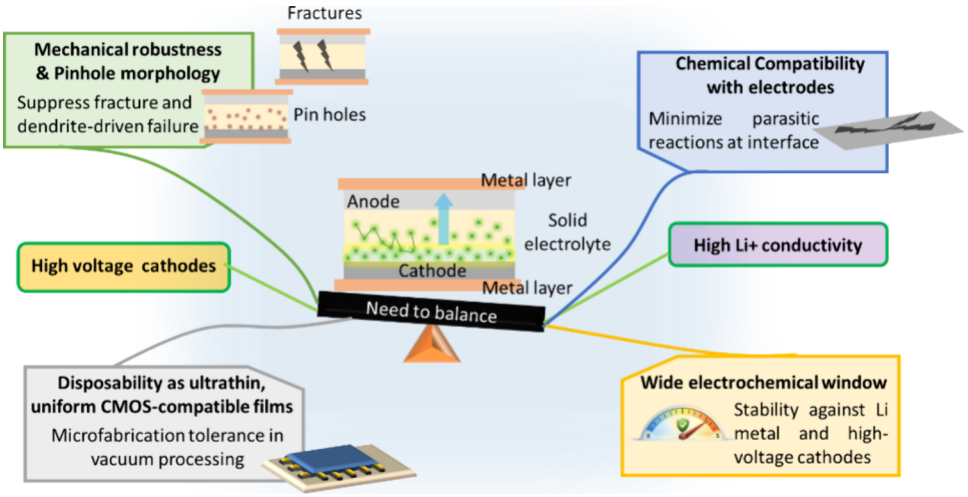

Figure 1. Conceptual framework illustrating the multiparameter design space governing ideal TFSEs.

(ALD), and chemical vapor deposition (CVD), imposes distinct kinetic and thermodynamic growth conditions which result in different ion dynamics in thin-film SE (TFSE). These deposition-parameter-dependent changes are not yet fully understood. While recent development using depth-resolved and operando characterization techniques has fundamentally reshaped the understanding of ion transport in TFSEs. These techniques include in situ X-ray diffraction,[12] Raman spectroscopy,[13] cryogenic transmission electron microscopy (Cryo-TEM),[14,15] scanning transmission electron microscopy (STEM) coupled with electron energy-loss spectroscopy (EELS),[16−20] and time-of-flight secondary ion mass spectrometry (TOF-SIMS).[21] All these studies revealed that TFSSB performance is not only governed by intrinsic electrolyte properties. But, it is critically also dependent on nanoscale phenomena such as space-charge effects, interphase evolution, defect-mediated Li^+ pathways, and mechanically driven failure modes under cycling.[12,13,22−24] Moreover, in TFSE, where the thickness is in few nanometers, the interfaces dominate volume. This will result in definitive alteration of film density, framework connectivity, and interfacial energetics with slight change in deposition parameters, which leads to change in ionic mobility and electrochemical stability.

In this Spotlight article, we mainly focus on TFSEs as the central materials bottleneck and opportunity for next-generation TFSSBs, where different deposition techniques are discussed. While the particular emphasis on PLD as a highly controllable and chemically versatile fabrication platform was highlighted. By correlating deposition conditions with the properties of TFSEs, such as film structure, ionic transport, and interface stability, with the insights from operando XRD, STEM-EELS, Cryo-TEM, Raman spectroscopy, and TOF-SIMS, this article outlines principles and research pathways spanning atomic-scale materials engineering to fully integrated micro-battery systems. Through this perspective, we aim to articulate a coherent roadmap for the development of next-generation TFSSBs tailored for high-performance and manufacturable microscale technologies.

Functional Requirements of Thin-Film Electrolytes in TFSSBs

TFSEs occupy a distinctive scientific and technological position within solid-state electrochemistry, where electrolyte thicknesses reduced to tens−hundreds of nanometers give rise to transport, interfacial, and mechanical phenomena that are fundamentally inaccessible in bulk materials. Under such extreme dimensional confinement, classical descriptions of ion migration, defect formation, and fracture mechanics no longer apply, and instead new behaviors emerge that are governed by nanoscale connectivity, interfacial energetics, and substrate constraint.[10,25−28] These effects enable microscale and on-chip battery architectures that cannot be realized using any conventional bulk SEs, positioning TFSEs as an enabling components for TFSSBs. Consequently, the viability of TFSEs (see Figure 1) is governed by a stringent convergence of properties, including sufficiently high Li^+ conductivity (~10^{-6} to 10^{-4} S cm^{-1}) to sustain rapid charge transport across submicrometer layers, a wide electrochemical stability window (~0 to 5 V vs Li/Li^+), mechanical robustness with pinhole-free morphology to prevent fracture and short-circuiting under extreme confinement, chemical compatibility with both Li metal and high-voltage cathodes, and the ability to be deposited as ultrathin, and uniform films which are fully compatible with CMOS microfabrication workflows.

At nanometer-scale thicknesses, TFSEs act not only as separators that prevent short-circuiting but also as functional layers that define the kinetic limits of the entire device.[29,30] The drastic reduction in Li^+ diffusion length allows high-rate operation even when the intrinsic ionic conductivity of the electrolyte is relatively modest.[31−33] At the same time, vacuum-based deposition techniques, most notably sputtering, PLD, and ALD, enable unprecedented control over glass-network organization, defect chemistry, and atomic-scale compositional uniformity.[5,34−36] These growth routes yield a TFSE thin film which is dense, grain-boundary-free, and fully amorphous films. It results in elimination of space-charge bottlenecks and provide short, and homogeneous ion-transport pathways. While the controlled incorporation of network modifiers such as nitrogen, oxygen, and halogens further enables fine tuning of local bonding environments and Li^+ hopping energetics. LiPON remains the archetypal demonstration of these principles.

The work by Bates, Dudney, and co-workers on LiPON has established that nitrogen incorporation results in restructuration of the phosphate network to create favorable Li^+ hopping sites without inducing crystallinity.[5,8,37] The resulting continuous amorphous framework removes mechanically and electrochemically weak intergranular regions, which account

https://doi.org/10.1021/acsaelm.6c00171
ACS Appl. Electron. Mater. 2026, 8, 4855−4875

for the exceptional stability of LiPON against metallic lithium, and it further helps to resist dendrite penetration. Beyond transport, TFSEs in microscale architectures also play a critical interfacial role by suppressing parasitic redox reactions, limiting cross-diffusion of mobile species, and stabilizing chemically abrupt interfaces with both Li metal anodes and high-voltage cathodes.[38−40] Achieving these functions relies on the deposition of dense, and pinhole-free layers with low defect densities, a requirement that is further strengthened by vacuum-integrated sequential processing, which minimizes interfacial contamination. In this regard, LiPON exhibits a broad electrochemical stability window of approximately 0–5 V vs Li/Li^+[41,42] and has demonstrated remarkable durability over $>10^4$ cycles in vacuum-assembled microbattery stacks.[43,44] Comparable interfacial stability has also been reported for amorphous PLD-grown Li_3PO_4 films, which remain stable up to ∼4.7 V, as confirmed by XPS and TEM analyses showing minimal interfacial degradation.[45−48]

Moreover, the mechanical robustness represents an equally critical requirement for long-term TFSSB reliability. Extreme dimensional confinement amplifies stresses arising from substrate constraint and thermal-expansion mismatch, particularly when electrolytes are deposited on rigid silicon or metallic current collectors[49−52]. In this regime, many crystalline oxide electrolytes exhibit increased stiffness and brittleness, leading to fracture, delamination, or electrically catastrophic short circuits at modest strain levels.[51−53] However, the amorphous electrolytes provide a clear advantage by accommodating strain without initiating microcracks. Due to this amorphous nature, they maintain a uniform mechanical barrier against Li intrusion. LiPON, ultrathin LLZO and LAGP films exemplify this behavior. But the LLZO and LAGP require adhesion layers or thermal conditioning to avoid mechanical failure.[54−56] A similar behavior is also observed in case of ALD-grown lithium polyphosphazene electrolytes with roughness <2 nm. Thus, atomically smooth surface correlates strongly with enhanced resistance to dendrite penetration.[57]

The TFSEs must be fully compatible with semiconductor and microfabrication workflows. They must tolerate sequential vacuum deposition, lithographic patterning, and thermal treatments typical of CMOS and MEMS processing without compositional drift, structural degradation, and interfacial failure.[3,58,59] This requirement restricts viable electrolytes to materials that are stable under vacuum, patternable at the microscale, and robust against thermal cycling. LiPON remains the benchmark material in this regard, while phosphate glasses and selected oxide systems, such as LLZO and LAGP, show steadily improving, but still incomplete, compatibility.[42,60,61] In contrast, sulfide electrolytes, despite their high intrinsic ionic conductivities, are fundamentally incompatible with microfabrication environments due to rapid degradation under vacuum and extreme moisture sensitivity.[62,63] Consequently, unlike bulk SEs, TFSEs must simultaneously satisfy stringent electrochemical, mechanical, and process-integration constraints, making the identification of universally viable material systems exceptionally challenging.

Why PLD Is Advantageous for Thin-Film Electrolytes

The performance of TFSEs in TFSSBs is mainly governed fundamentally by the deposition strategy employed. Film stoichiometry, microstructure, defect population, and interfacial integrity are not only intrinsic material constants but also emerge from the thermodynamic and kinetic boundary conditions imposed during growth. Consequently, the choice of fabrication technique exerts first-order control over ionic conductivity, electrochemical stability, and long-term device reliability. Across more than five decades of TFSSB research from early AgI/LiI thin films to contemporary LiPON, garnet, NASICON, and hybrid electrolytes, three deposition categories have consistently demonstrated the ability to meet the stringent requirements of nanoscale uniformity, chemical precision, and interfacial cleanliness, which are sputtering,[47,64−74] PLD,[23,45,75−90] and ALD[57,91−99] (see Figure 2). These physical vapor and surface-limited techniques enable dense, pinhole-free films with nanometer-scale thickness control, which makes them uniquely compatible with microscale and three-dimensional battery architectures.

Among these methods, PLD occupies a distinctive niche for complex inorganic electrolytes. Its laser-driven ablation process enables near-congruent transfer of multicomponent targets, which is a decisive advantage for lithium-containing oxides such as Li_3PO_4, LLZO, and NASICON-type materials. Table 1 discusses all the PLD parameters that influence ablation behavior, plume dynamics, reactive nitridation, and film microstructure in oxide

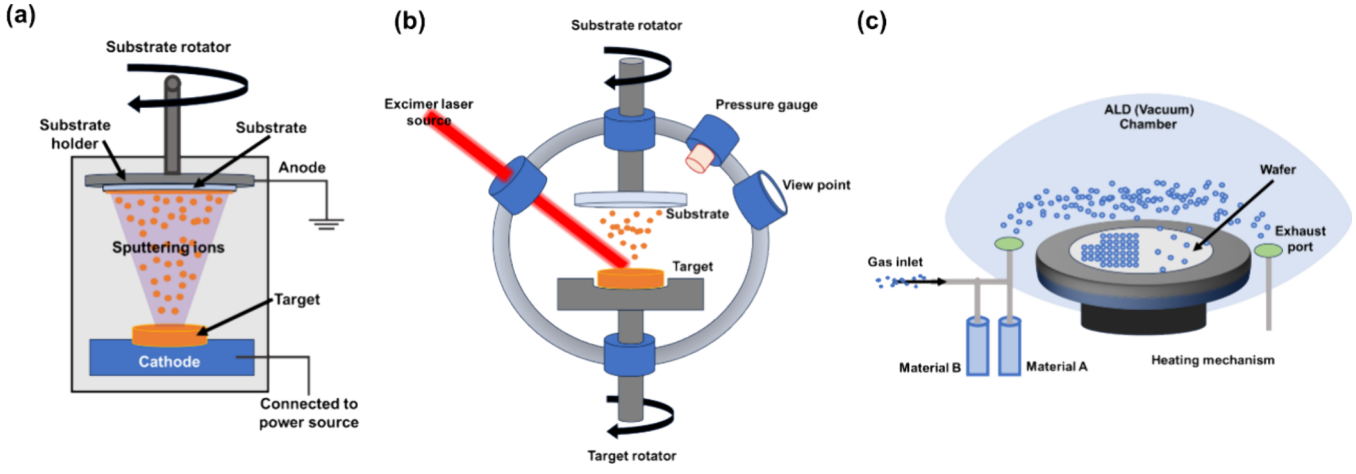

Figure 2. Schematic representation of the three thin-film deposition techniques examined in this work: (a) sputtering, (b) PLD, and (c) ALD.

https://doi.org/10.1021/acsaelm.6c00171
ACS Appl. Electron. Mater. 2026, 8, 4855−4875

Table 1. PLD Parameters Influencing Ablation Behavior, Plume Dynamics, Reactive Nitridation, and Film Microstructure in Oxide and Oxynitride TFSEs

parameter	influence on deposition	characteristics/evidence
laser fluence (energy density)	the laser fluence governs the ablation rate, plume energy, and extent of reactive nitrogen incorporation into the film, where the higher fluence result in increase of both deposition rate and nitrogen uptake but can also promote particulate formation when excessively high	effective fluence values for LiPON[131] range from 5 to 20 J cm^{-2}, where it is observed that the conductivity increases with fluence and saturates above ∼15 J cm^{-2}, while fluence values above this threshold significantly increase droplet formation[131]
laser wavelength	the laser wavelength determines the absorption depth and ablation efficiency of the target, where the shorter wavelength enables more efficient and cleaner material removal. While laser spot size influences ablation uniformity and target utilization	LiPON PLD has been demonstrated using 355 nm ultraviolet radiation[131] from a Nd:YAG laser, and UV wavelengths are generally preferred for oxide systems due to their higher absorption and reduced thermal effects[84,88,132−135]
pulse repetition rate	the repetition rate controls the average deposition rate and influences plume−substrate interaction frequency, thereby affecting film growth kinetics	typical repetition rates for PLD are within 1−10 Hz, where for a LiPON film growth, generally a 10 Hz repetition rate is taken[131]
background gas and pressure	the type and pressure of background gas regulate plume expansion, reactive nitridation, oxidation state, and the degree of amorphization in the growing film. Thus, higher nitrogen pressure increases nitrogen incorporation but also contracts the plume and lowers deposition rate	for LiPON deposition, nitrogen pressures between 50 and 200 mTorr enhance nitrogen incorporation, leading to increased conductivity, whereas excessive pressure reduces deposition efficiency due to plume scattering[131]
substrate temperature	the substrate temperature dictates crystallinity, phase formation, and densification of the deposited film, where lower temperatures favour amorphous structures, while higher temperatures promote crystalline formation	LiPON films deposited near room temperature form amorphous phases with high ionic conductivity[131]
target−substrate distance	influences uniformity, deposition rate, and particulate density such that larger distances reduce droplet contamination and stabilize film morphology	increasing the target−substrate distance to 5 cm will result in minimization of particulate contamination while it also help to preserve an adequate deposition rate for smooth PLD-LiPON film[131]

and oxynitride TFSEs. The high kinetic energy of ablated species promotes dense microstructures and facilitates stabilization of metastable and highly ordered oxide networks at comparatively low substrate temperatures. As a result, PLD has emerged as one of the few techniques capable of producing crystalline garnet and NASICON thin films with technologically relevant ionic conductivities following appropriate post-deposition annealing.[78,100−106] In contrast, sputtering represents the most technologically mature and scalable route for amorphous TFSEs.[47,64−74] RF and magnetron sputtering underpin the widespread adoption of LiPON, where reactive N_2 plasmas enable controlled nitrogen incorporation. This yields electrolytes with excellent electrochemical stability and full compatibility with CMOS and MEMS processing.[47,65,74,107−113] While sputtering has been extended to more complex oxides, such as LAGP, LATP, and LLZO, via reactive and high-power impulse configurations.[47,65,74,107−113] However, sputtering frequently suffers from lithium volatility and phase purity remains challenging for multicomponent crystalline electrolytes.[45,75−78,83,88−90]

Other techniques like ALD defines the opposite end of the process spectrum, which offers angstrom-level thickness control and unmatched conformality through self-limiting surface reactions.[57,91−99] Thermal and plasma-enhanced ALD have enabled ultrathin amorphous electrolytes, such as LiN_xO_y, $Li_2O−Al_2O_3$, Li_3BO_3, as well as LiPON-like oxynitride films, which show excellent mechanical compliance and interfacial stability.[57,91−99] However, slow growth rates and limited lithium precursor options continue to constrain throughput and materials diversity. Alternative fabrication routes, including chemical vapor deposition (CVD), electrochemical deposition, solution-based processing, mechanical deposition, and printing have been explored to address scalability and cost.[114−124] However, these approaches generally fail to simultaneously satisfy the combined demands of nanometer-scale thickness control, stoichiometric fidelity, and interfacial cleanliness required for high-performance inorganic TFSEs. Such as CVD methods are restricted by the scarcity and instability of volatile lithium precursors, elevated processing temperatures, plasma-induced damage, and carbon contamination.[116,120−128] While electrochemical deposition struggles to produce lithium-containing oxides and often yields moisture-sensitive films.[116,120−128] Moreover, solution-based and printing techniques frequently suffer from porosity, cracking, nonuniform drying, and poor edge control,[116,120−128] while mechanical deposition and additive manufacturing lack the resolution required for ultrathin films.[118,119,129,130]

Based on the reports on fabrication of TFSEs, only three deposition techniques, such as sputtering, PLD, and ALD, constitute the most reliable and versatile fabrication methods. Each technique has its benefits, such as sputtering is good for scalable amorphous electrolytes, PLD is for stoichiometrically complex and crystalline oxides, and ALD for conformal ultrathin coatings. These benefits underscore the need to match deposition physics with electrolyte chemistry, target thickness, and device architecture. Despite major progress, several challenges remain unresolved, too in different deposition techniques. Such as the scalable routes for crystalline lithium garnet and sulfide TFSEs with precise stoichiometry are still lacking. While the lithium precursor chemistry limits both ALD and CVD expansion. In the case of PLD, the scalability and particulate formation remain concerns for industrial translation. Addressing these gaps is essential to further develop TFSE, which requires hybrid deposition strategies, advanced in situ diagnostics, and closer integration between deposition science and device-level engineering, as further discussed in this spotlight article.

Microstructure and Defect Control in PLD-Grown Electrolytes

PLD occupies a unique position among thin-film techniques owing to its ability to reproduce complex target stoichiometry, stabilize metastable phases, and generate dense amorphous as well as crystalline networks (Figure 2b).[85,87−89,134−136] Short, and high-energy laser pulses, typically from excimer or

https://doi.org/10.1021/acsaelm.6c00171
ACS Appl. Electron. Mater. 2026, 8, 4855−4875

Nd:YAG sources, induce rapid target ablation and formation of a highly energetic plasma plume that condenses on a heated substrate, often with near-congruent transfer of multicomponent compositions. This energetic growth environment enables dense microstructures and crystallization at comparatively low substrate temperatures, making PLD particularly effective for oxide electrolytes such as Li_3PO_4, LLTO, LLZO, and NASICON-type materials,[78,100−106] which is further detailed in Table 2. However, the electrochemical performance of PLD TFSEs is governed less by its intrinsic bulk chemistry, but it largely depends on deposition-induced microstructure.

Comparative studies across a broad library of oxide and glass-ceramic electrolytes, including Li_3PO_4, $LiBO_2$, Li_2SiO_3, Li_2SO_4, $LiAlO_2$, and Li_2WO_4, demonstrate a consistent trend. Such that the large laser photon energies promotes dense, continuous, and pinhole-free films, while lower-energy irradiation yields rough, droplet-rich, and discontinuous layers.[84,88,132−135] The dense microstructures maximize the connectivity of fast-ion percolation networks and suppresses the parasitic electronic conduction pathways. While the porous and cracked films suffered with diminished ionic conductivity, degraded mechanical integrity, and interfacial instability. Thus, the laser photon energy emerges as a pivotal and broadly universal control knob.

Table 2. Comparison of Key Properties of PLD-Fabricated TFSEs

electrolyte	ionic conductivity (S/cm) and activation energy (eV)	electro-chemical window vs Li (V)	PLD conditions	film thick-ness	ref
$Li_xPO_yN_z$ (LiPON)	1.6×10^{-6} and 0.58 eV	0–5.5	Nd:YAG laser (Spectra Physics, GCR-190) laser and repetition rate 10 Hz.	2.4−3 μm	131
Li_3PO_4	4.5×10^{-7} and 0.6 eV	0–4.7	ArF excimer laser (Coherent COMPexPro 102) and 5 Hz	1.5 μm	134
	1.02×10^{-8}	3.0–4.3	ArF excimer laser and 5−20 Hz	50 nm	137
		2.5–4.5	ArF excimer laser	1.0 μm	138
	4.6×10^{-7} and 0.57 eV		ArF excimer and 5 Hz		83
Li_4SiO_4−Li_3PO_4	1.6×10^{-6}	0–3.6	KrF excimer laser and 10 Hz	∼1.0 μm	139
$Li_{3.4}V_{0.6}Si_{0.4}O_4$	3×10^{-7} and 0.54 eV	0.5–3.0	Q-switched Nd:YAG laser and 10 Hz	2.5 μm	135
$Li_{6.4}La_3Zr_{1.4}Ta_{0.6}O_{12}$	0.67 ± 0.05 eV (above 673 K) and 1.1 ± 0.2 eV (below 673 K)		Nd:YAG laser and 10 hz	2−5 μm	103
$Li_{3.25}Ge_{0.25}P_{0.75}S_4$	1.7×10^{-4} and 0.38 eV		KrF excimer laser and 10 Hz	3.2 μm	77
$(Li_{0.5}La_{0.5})TiO_3$	2.0×10^{-5} and	3.3–4.0	4 Hz	360 nm	140
$Li_{3x}La_{1/3-x}TaO_3$, $x = 0.075$	0.2×10^{-6}−1.5×10^{-6} and 0.41−0.49 eV		Lambda Physik COMPex 205 excimer laser and 10 Hz	359−409 nm	141
Li_2O-Si_2O (LSO)	2.2×10^{-4} and 0.72−0.79 eV		KrF and Nd:YAG laser	0.15 μm	142
β-$LiAlSiO_4$	$\sim 8 \times 10^{-5}$ and 0.87 eV		KrF excimer laser (LAMBDA PHYSIK) and 10 Hz	1.2 μm	143
	10^{-4}−10^{-5}		K rF excimer laser and 10 Hz	0.0075−1.2 μm	144
$Li_6BaLa_2Ta_2O_{12}$	2×10^{-6} and 0.42 eV	0–4.2	KrF-laser (Compex 201 F, Coherent and 10 Hz	200 nm	76
$80Li_2S{\cdot}20P_2S_5$	7.9×10^{-5}		KrF excimer laser (LPXPro, Lambda Physik, Santa Clara) and 10 Hz	3.0 μm	145
$Li_7La_3Zr_2O_{12}$ (LLZO)	2.0×10^{-6}(001) and 1.0×10^{-5}(111)		KrF excimer laser and 5–20 Hz	26.2 nm (001) and 30.4 nm (111)	146
	3.35×10^{-7}		KrF excimer laser and 10 Hz		147
	3.54×10^{-6}		KrF excimer and 5 Hz	100 nm	148
	7.19×10^{-8} and 0.45 eV		KrF excimer laser and 10 Hz	1 μm	149
$Li_7La_3Zr_2O_{12} + Li_2O$	1.78×10^{-7}−7.36×10^{-7} and 0.32−0.41 eV		KrF excimer laser and 10 Hz	1 μm	149
$Li_7La_3Zr_2O_{12} + LiOH$	1.1×10^{-2}		KrF excimer and 5 Hz	100 nm	148
$Li_{1.3}Al_{0.3}Ti_{1.7}(PO_4)_3$ (LATP)	10^{-7} to 10^{-6} and 0.37−0.53 eV	2.8–4.5	KrF excimer laser (Coherent COMPex PRO) and 50 Hz	<1 μm	111
Ta-doped $Li_7La_3Zr_2O_{12}$ (Ta-LLZO)		0.05–5	KrF excimer laser and 10 Hz	330 nm	150
$Li_{6.75}La_3Zr_{1.75}Ta_{0.25}O_{12}$			Nd:YAG laser source (Handy YAG Quanta System Q-switched) and 10 Hz	500−700 nm	100
LL(Nb,Ti)O-(Ti, Nb)O_2	2.3×10^{-4} and 0.27 eV		KrF excimer laser and 5 Hz	100 nm	151
La_2LiHO_3	1.3×10^{-8} and 0.46 eV		Nd:$Y_3Al_5O_{12}$ solid-state laser		152
$Li_{4-x}Ge_{1-x}P_xO_4$ (LGPO)	$1-10 \times 10^{-6}$ and 0.60 eV	−0.5 to 7	KrF excimer laser and 10 Hz	150−300 nm	153
	$\sim 10^{-5}$ and 0.47 eV		KrF excimer laser (LAMBDA PHYSIK LPX 300) and 10 Hz	100−250 nm	154
Li_2SiO_3	2.5×10^{-8} and 0.64 eV	3.0−4.4	ArF excimer laser and 5 Hz	2.7 μm	155
	1.3×10^{-8} and 0.64 eV		ArF excimer and 5 Hz		83
	$1.1-4.5 \times 10^{-4}$ and 0.78−0.94 eV		Nd:YAG laser	0.08−0.15 μm	156
			Nd:YAG laser	0.03−0.47 μm	157
Li_2WO_4	1.0×10^{-3} and 0.20 eV		ArF excimer and 5 Hz		83
Li_2SO_4	5.4×10^{-8} and 0.62 eV		ArF excimer and 5 Hz		83
$LiBO_2$	2.8×10^{-9} and 0.68 eV		ArF excimer and 5 Hz		83
ohara glass	1.6×10^{-10} and 0.69 eV		ArF excimer and 5 Hz		83
$LiTaO_3$ perovskite-oxide			KrF excimer laser and 4 Hz	340 nm	81,158

https://doi.org/10.1021/acsaelm.6c00171
ACS Appl. Electron. Mater. 2026, 8, 4855−4875

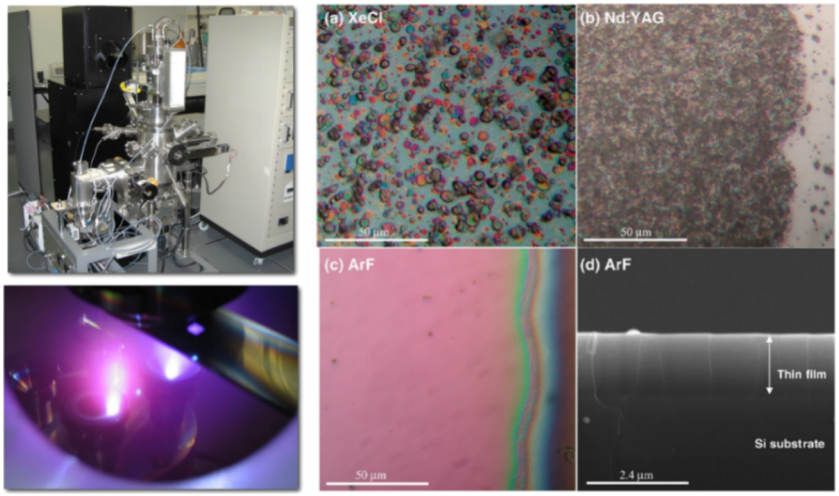

Figure 3. Typical PLD system and the plume during film deposition. Panels (a–c) present optical micrographs of Li_3PO_4 films produced using the fourth harmonic of an Nd:YAG laser, an ArF excimer laser, and a XeCl excimer laser, respectively. Panel (d) provides a cross-sectional FE-SEM image fabricated with the ArF excimer source. Reproduced or adapted with permission from ref 83. Copyright [2009] [Elsevier].

Though laser photon energy, film density, morphology, defect landscapes, and ultimately lithium-ion transport can be easily controlled. This microstructure-centric paradigm with laser energy is especially evident in wide-band-gap oxide electrolytes, where subtle differences in plume energetics translate into orders-of-magnitude changes in ionic conductivity. These observations establish laser energetics as a generalizable design parameter for PLD-grown TFSEs.

Moreover, the properties of TFSEs are also dependent on laser wavelength. Kuwata et al. demonstrated that laser wavelength, and therefore photon energy, directly govern both film morphology and lithium-ion transport (Figure 3).[83] High-energy ArF excimer irradiation (193 nm, 6.4 eV) produces smooth, dense, and homogeneous amorphous films, whereas lower-energy Nd:YAG (266 nm) and XeCl (308 nm) sources generate rough surfaces populated by micron-scale droplets. As a direct consequence of this morphological control, ArF-deposited Li_3PO_4 exhibits a room-temperature ionic conductivity of $\sim 4.6 \times 10^{-6}$ S cm^{-1} with an activation energy of ~0.57 eV, nearly two orders of magnitude higher than films grown with longer-wavelength lasers.[83] The superior performance of ArF-PLD films is attributed to more efficient photon absorption at the target surface, reduced splashing and particulate ejection, and stabilization of a dense amorphous phosphate network favorable for Li^+ migration. Similar wavelength-dependent effects have since been reported for amorphous Li_2O-SiO_2, $Li_4SiO_4-Li_2SiO_3$ films, and LiPON-related compositions,[84,142,144,155] confirming that short-wavelength, high-photon-energy excitation is a powerful route to microstructural optimization in oxide TFSEs. Figure 3 schematically illustrates a typical PLD setup and plume evolution, while Figure 3a–d directly correlates laser source with Li_3PO_4 film morphology and cross-sectional density.[83]

Further, the substrate temperature and post-deposition annealing offer effective secondary levers for tailoring density and interfacial chemistry. These parameters introduce additional degrees of freedom for tailoring electrolyte microstructure and interfacial chemistry. For amorphous perovskite electrolytes, such as LLTO, growth at intermediate temperatures (400–600 °C) followed by rapid thermal annealing near 700 °C has been shown to improve capacity retention in SSBs. This is attributed primarily to interfacial restructuring and reduction of contact resistance rather than dramatic enhancement of bulk ionic conductivity.[159] Such that the thermal treatment facilitates interdiffusion at electrode–electrolyte interfaces, which promote intimate contact and reduce interfacial impedance. In contrast, for sulfide-based films, such as thio-LISICON compositions (e.g., $Li_{3.25}Ge_{0.25}P_{0.75}S_4$) and lithium thiophosphate glasses ($80Li_2S{\cdot}20P_2S_5$), low-temperature deposition is essential to preserve the amorphous and glassy structure.[77,145] Though the moderate post-annealing (typically 200–300 °C) can beneficially increase local structural order and improve percolation network connectivity without inducing crystallization and grain boundary formation. Ohta et al. illustrate this delicate balance between maintaining glassy disorder for low activation energy in PLD thio-LISICON films. It also introduces sufficient short-range order to enhance carrier mobility, which achieves conductivities exceeding 10^{-3} S·cm^{-1} at room temperature.[77] Also, the importance of film density cannot be overstated, too, as pinholes and cracks not only provide short-circuit paths for electrons (reducing coulombic efficiency) but also expose reactive electrode materials to each other, leading to interfacial degradation and capacity fade. Moreover, the film thickness and substrate selection introduce yet another layer of complexity, particularly for ultrathin electrolytes where interfacial effects dominate. Reducing electrolyte thickness is a straightforward strategy to minimize ohmic drop and enable high-rate operation. However, ultrathin films are highly susceptible to substrate interactions that can either enhance or degrade performance. A high ionic conductivity and electronic insulation were maintained for a 15 nm PLD LiPON film on ion-blocking substrates, such as Pt or TiN, which prevent Li exchange and preserve stoichiometry throughout the electrolyte layer.[160−162]

Conversely, when nonblocking oxide substrates like TiO_2 are employed, lithium out-diffusion occurs during deposition (driven by the temperature and chemical potential gradient) or during subsequent annealing, creating a lithium-depleted

https://doi.org/10.1021/acsaelm.6c00171
ACS Appl. Electron. Mater. 2026, 8, 4855−4875

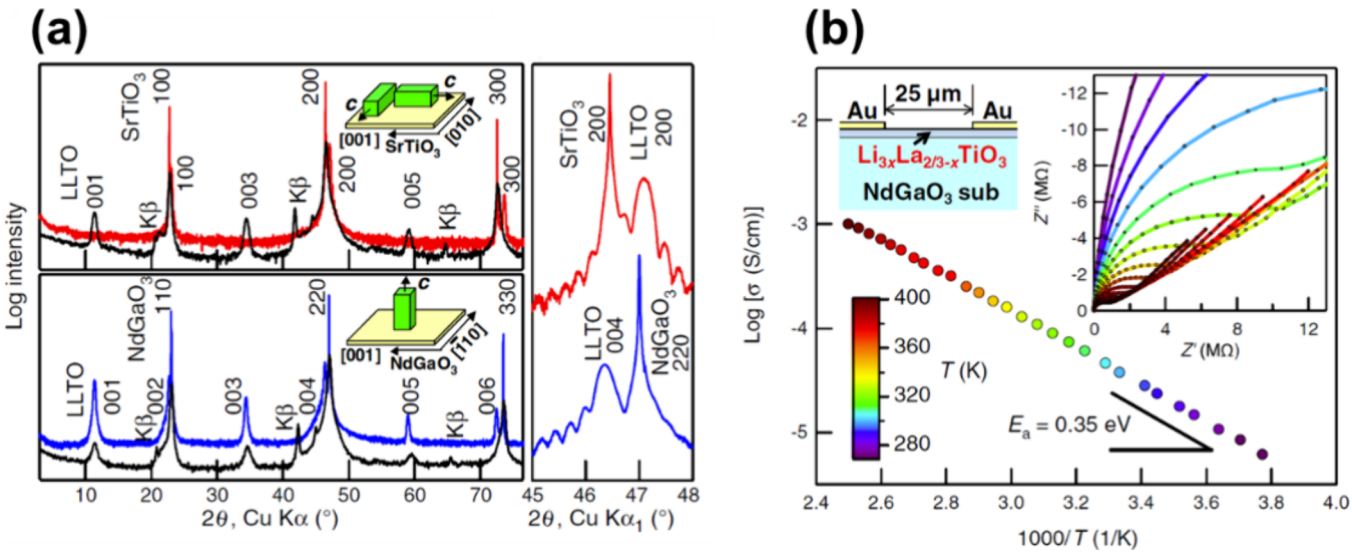

Figure 4. XRD profiles of LLTO films deposited on $SrTiO_3$(100) and $NdGaO_3$(110), showing both wide-range and magnified out-of-plane scans, together with in-plane diffraction data. The accompanying schematics indicate the corresponding *c*-axis orientations on each substrate. (b) Temperature-dependent in-plane ionic conductivity of a 36-nm LLTO film on $NdGaO_3$(110), with Nyquist plots and the measurement geometry provided in the inset. Reproduced or adapted with permission from ref 22. Copyright [2012] [Elsevier].

interfacial region with reduced carrier concentration and therefore lower effective ionic conductivity.[163,164] Ohnishi and Takada[22] demonstrated the controlled growth of epitaxial LLTO thin films by PLD, establishing the processing conditions necessary to probe intrinsic Li-ion transport in this perovskite electrolyte. Because Ti must be preserved in the Ti^{4+} state to stabilize the lattice, crystallization occurs only under stringent conditions, temperatures exceeding 900 °C and oxygen pressures above 5 Pa, with fully optimized growth achieved at 1050 °C and 10 Pa O_2. Under these settings, the films exhibit layer-by-layer growth, confirmed through RHEED oscillations and AFM-observed terrace structures. Figure 4a showed that how the substrate choice dictates epitaxial orientation. On $SrTiO_3$(100), LLTO forms a two-domain in-plane *c*-axis configuration, whereas on $NdGaO_3$(110), it adopts a predominantly out-of-plane *c*-axis alignment. The LLTO film grown on $NdGaO_3$ approaches a single-domain state and enables more reliable assessment of directional ion transport. Figure 4b presents the temperature-dependent in-plane conductivity of a 36-nm film on $NdGaO_3$, revealing Arrhenius behavior with an activation energy of 0.35 eV and a room-temperature conductivity of ~3.5×10^{-5} S cm^{-1}. Although lower than bulk intragrain values, likely due to epitaxial strain and Li deficiency arising from preferential scattering of light Li species during PLD, the films provide a robust platform for examining anisotropic Li-ion motion and inform strategies for optimizing next-generation TFSEs. A similar substrate mismatching condition is utilized in LLZO where substrates with different crystallographic orientations are used to deposited (001) and (111) orientations LLZO. Kim et al. reported the first successful synthesis of epitaxial Al-doped LLZO thin films with controlled (001) and (111) orientations on $Gd_3Ga_5O_{12}$ substrates using PLD, enabling direct evaluation of lithium-ion transport within single-crystal grains without grain-boundary effects.[146] Structural characterization (XRD and XRR) confirms high-quality epitaxy with slight lattice distortions that differ between orientations, while ICP-MS reveals significant Al incorporation (≈0.65−0.71 mol), which compensates lithium loss during deposition and substitutes for Li sites in the garnet lattice. This Al substitution reduces the concentration of mobile Li^+ and disrupts the three-dimensional migration network, which leads to markedly lower ionic conductivities compared to bulk LLZO, where the conductivity is 2.5×10^{-6} S cm^{-1} for LLZO (001) and 1.0×10^{-5} S cm^{-1} for LLZO (111) at room temperature. The Arrhenius behavior shown in Figure 5 demonstrates activation energies of 50–53 kJ mol^{-1}, and the higher conductivity of the (111) film is attributed to its smaller lattice misfit and reduced strain relative to the (001) film. This substrate-induced compositional gradient can extend several nanometers into the electrolyte, which leads to effective increasing the resistive thickness.

There are some post-deposition processes that can also affect the ionic conductivity. For example, Rawlence et al. investigated how post-lithiation influences the phase stability and microstructural evolution of pulsed-laser-deposited Al-stabilized LLZO thin films on MgO, revealing that lithium incorporation is strongly thickness-dependent and directly governs both morphology and functional performance.[102] As shown in Figure 6, films below ~90 nm lithiated effectively and crystallize into cubic LLZO but form discontinuous de-wetted islands, while intermediate films near 110 nm exhibit mixed cubic/tetragonal phases with partially connected morphologies. For thicker films (≥130 nm), lithium incorporation becomes insufficient, leading to dense but predominantly Li-deficient $La_2Zr_2O_7$−LLZO mixtures. These structural transitions highlight a trade-off such as thinner films achieve the desired cubic garnet phase but lack film continuity, whereas thicker films provide dense, processable layers but lose lithium and transform into less conductive impurity phases. Electrochemical impedance spectroscopy (EIS) shows that a 380-nm film delivers a bulk ionic conductivity of 1.2×10^{-3} S cm^{-1} at 325 °C, despite dual activation energies reflecting mixed-phase conduction pathways. Collectively, the work establishes that the post-deposition treatment of cubic LLZO in thin films is tightly linked to lithiation efficiency,

https://doi.org/10.1021/acsaelm.6c00171
ACS Appl. Electron. Mater. 2026, 8, 4855−4875

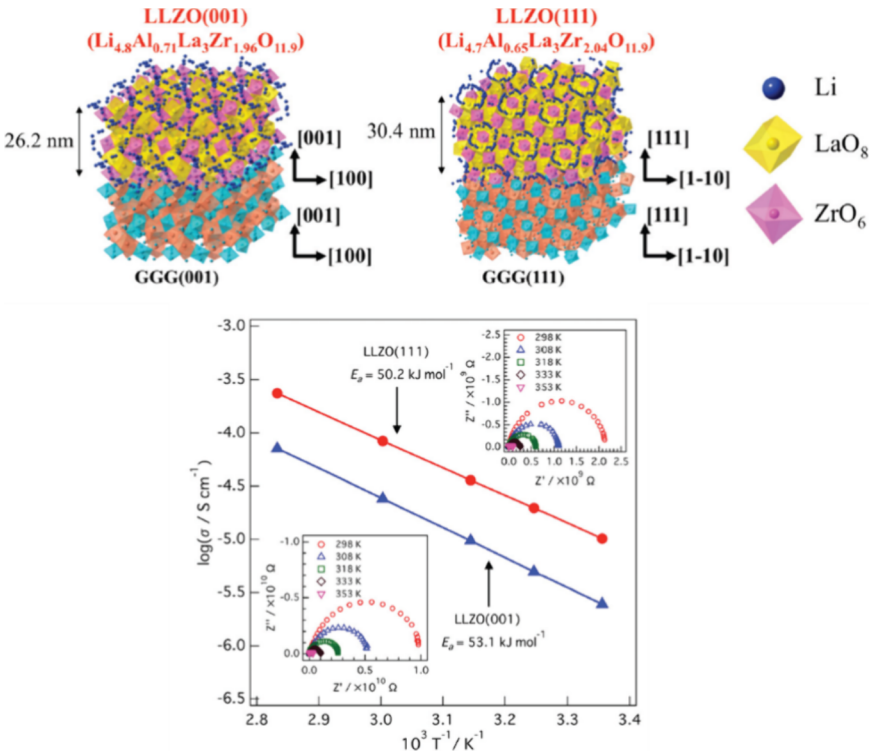

Figure 5. Structural characterization and compositional analysis of epitaxial LLZO films grown on GGG (001) and GGG (111) substrates. The accompanying Arrhenius plots compare ionic conductivities measured along the [110] direction for LLZO (001) and the [112] direction for LLZO (111). Insets display representative impedance spectra collected at different temperatures. Reproduced or adapted with permission from ref 146. Copyright [2013] [RSC Publishing].

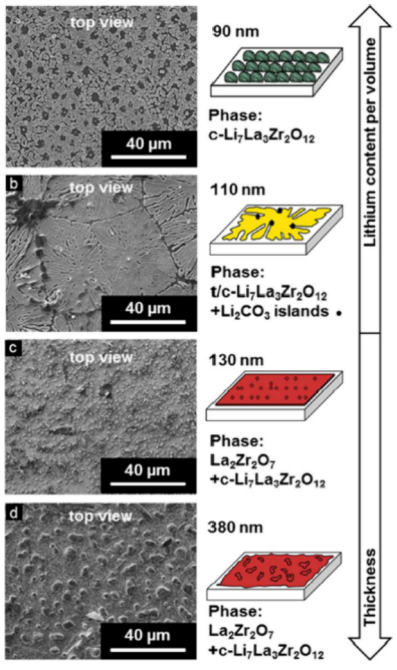

Figure 6. SEM images of LLZO thin films with progressively increasing thickness, (a) 90 nm, (b) 110 nm, (c) 130 nm, and (d) 380 nm, illustrate the evolution of surface and structural features as the films grow thicker. The accompanying schematic drawings highlight how both phase development and morphology change with thickness. Reproduced or adapted with permission from ref 165. Copyright [2017] [IOP Publishing].

underscoring the need to balance microstructure, phase purity, and Li retention when designing garnet-based TFSEs for future microbattery architectures.

Thus, these observations underscore the necessity of carefully matching substrate chemistry to electrolyte composition and processing conditions. Collectively, findings across Li_3PO_4, LiPON, perovskite, garnet, and sulfide TFSEs systems establish a unified, microstructure-centric design paradigm in which PLD parameters dictate electrolyte performance through three interrelated mechanisms: (i) stoichiometry and dopant incorporation, governed primarily by ambient gas chemistry and laser fluence;[23,131] (ii) defect chemistry, modulated by oxygen or nitrogen partial pressure and post-deposition thermal history;[140,166,167] and (iii) microstructure and film density, controlled by laser photon energy, substrate temperature, and annealing protocols.[23,84,142,144,155] This framework underscores a fundamental shift in the understanding of TFSEs, namely that ionic transport is not an intrinsic material constant but an engineered property arising from deposition physics. Consequently, precise control over laser energetics and the broader PLD parameter space enables the rational design of TFSEs with tailored ionic conductivity, interfacial stability, and electrochemical performance, positioning PLD as a uniquely powerful platform for the development of next-generation thin-film battery architectures.

Diffusion Analysis of PLD-Grown Electrolytes

In contrast to bulk SEs, where ionic diffusion has been systematically quantified using a combination of EIS, nuclear magnetic resonance (NMR), and time-of-flight secondary ion mass

https://doi.org/10.1021/acsaelm.6c00171
ACS Appl. Electron. Mater. 2026, 8, 4855−4875

spectrometry (TOF-SIMS), quantitative insight into diffusion processes in TFSEs remains remarkably sparse. For bulk materials, EIS provides indirect diffusion estimates through ionic conductivity, NMR yields self-diffusion coefficients, particularly effective in lithium-rich compositions, and TOF-SIMS enables spatially resolved visualization of ion migration, allowing separation of bulk, grain-boundary, and interphase transport pathways.[21] By comparison, diffusion studies in TFSEs architectures have largely remained confined to impedance-based analyses, leaving nanoscale transport mechanisms in ultrathin electrolytes poorly constrained. A notable exception is the seminal work of Kuwata et al., who established a rigorous and experimentally accessible framework for directly quantifying lithium tracer diffusion in amorphous Li_3PO_4 thin films. Using dense, crack-free a-Li_3PO_4 layers grown by PLD, the authors implemented stable-isotope ($^6Li/^7Li$) exchange combined with secondary ion mass spectrometry (SIMS) to overcome the limitations of conventional electrochemical probes.[133] Two complementary isotope-diffusion geometries were designed and schematically summarized in Figure 7a. First one is a vertical ion-exchange configuration, in which a ^6Li-enriched film is immersed in a natural-lithium electrolyte to generate a sharply defined isotopic interface normal to the film surface. While the second one is a lateral mask geometry, where a natural-Li overlayer is selectively deposited across a ^6Li film, enabling in-plane diffusion analysis along a well-defined interface, as shown in Figure 7b.

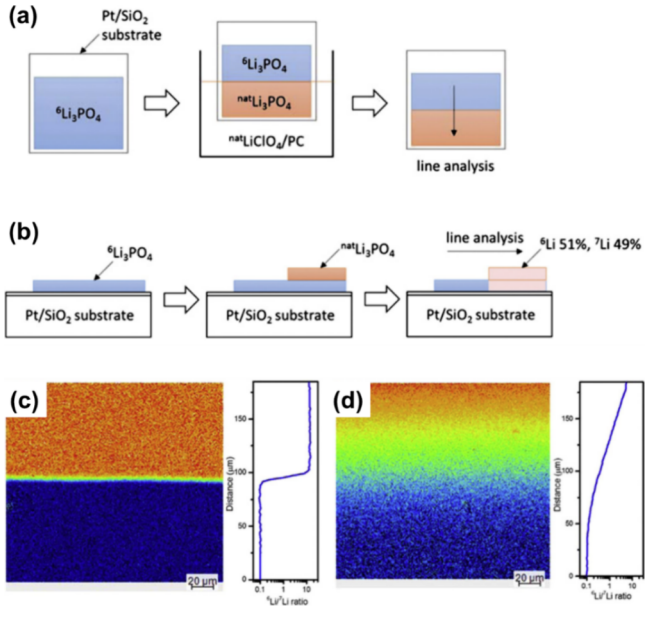

Figure 7. Schematic illustration of the two diffusion couple fabrication approaches: (a) the ion-exchange route, in which a ^6Li-rich a-Li_3PO_4 film is partially substituted with natural-Li by immersion in a $LiClO_4$/PC electrolyte, and (b) the mask-assisted deposition route, where a ^{nat}Li overlayer is patterned onto a ^6Li film. The resulting $^6Li/^7Li$ distributions were quantified using SIMS line profiling. Representative isotope maps for diffusion couples formed by the ion-exchange method are shown for (c) the as-prepared interface and (d) the sample after annealing at 120 °C for 24 h. All mappings were acquired over a 200 × 200 μm^2 scan area. Reproduced or adapted with permission from ref 133. Copyright [2016] [Elsevier].

SIMS isotope maps (Figure 7c,d) directly visualize lithium migration in these diffusion couples. The as-prepared samples show a sharp isotopic boundary below 10 μm. After annealing at 120 °C, this boundary broadens beyond 100 μm, which directly confirms Li^+ transport in real space. SIMS line profiles were then fitted using Fick's second law, which results in a room-temperature tracer diffusion coefficient of 6×10^{-13} cm^2 s^{-1} with activation energy ∼0.58 eV. These values are consistent for both diffusion geometries, which confirms the reliability of the method. It also indicates thermally activated hopping in a disordered phosphate network. Impedance spectroscopy gives $\sigma \sim 2.9 \times 10^{-7}$ S cm^{-1} at 25 °C, with activation energy ∼0.55 eV. The Haven ratio is ∼0.55 ± 0.20 from 25 to 160 °C. A value below unity indicates correlated lithium motion. This is typical for glassy phosphate electrolytes. Overall, isotopic mapping and diffusion analysis provide a robust framework, which links microscopic diffusion with macroscopic transport. This establishes a reliable approach to study Li^+ mobility in TFSEs. It also provides key insight for designing PLD-grown TFSEs in microbattery and TFSSB systems.

It is important to note that studies employing time-of-flight secondary ion mass spectrometry (TOF-SIMS) on TFSEs remain relatively scarce. In this context, selected investigations involving electrochemically active electrode materials are discussed to provide a broader perspective on ion transport and interfacial processes. These studies offer a conceptual framework from which analogous methodologies may be extended to TFSEs, enabling deeper insight into diffusion behavior and interfacial chemistry. As such, the active electrode materials necessarily function as mixed ionic−electronic conductors, in which lithium diffusion through the host lattice constitutes a rate-limiting process that is formally governed by the same Fickian transport framework applied to SEs. Kuwata et al. significantly broadened the scope of SIMS by applying it to spinel $Li_xMn_2O_4$ thin film cathodes, thereby demonstrating the generality of the approach for quantifying intrinsic lithium mobility in crystalline, electrochemically active materials.[168] Using a step−isotope-exchange SIMS methodology (Figure 8a), lateral position within a PLD-grown film is mapped to effective exchange time by sequential exposure to a ^6Li-enriched electrolyte. Representative isotope profiles obtained for $Li_{0.6}Mn_2O_4$ (Figure 8b,c) exhibit well-defined step-like features and yield a tracer diffusion coefficient $D^* \sim 3.5 \times 10^{-13}$ cm^2 s^{-1}. Systematic variation of lithium content (Figure 8d) uncovers a striking four-order-of-magnitude increase in D^* upon delithiation within the α-phase, quantitatively described by a vacancy-mediated diffusion model. In contrast, modest reductions in D^* across the β-phase and two-phase regions highlight the kinetic influence of lithium ordering, Li−Li repulsion, and phase-boundary traversal.[168] Similarly, the applicability of SIMS to anisotropic layered oxides was further demonstrated in Li_xCoO_2 thin films, where lithium diffusion along the crystallographic *c*-axis has long been debated.[169] The room-temperature tracer diffusion coefficients reveal that D^* spans nearly five orders of magnitude (∼10^{-17} to 10^{-12} cm^2 s^{-1}) across $0.4 < x < 1.0$ and collapses sharply near stoichiometry.[169] This behavior is quantitatively captured by a vacancy-blocking model in which Li mobility scales with $(1 - x)$. To reconcile finite *c*-axis diffusion with the absence of continuous diffusion channels through CoO_2 slabs, a physically grounded mechanism is proposed, wherein lithium ions migrate via

https://doi.org/10.1021/acsaelm.6c00171
ACS Appl. Electron. Mater. 2026, 8, 4855−4875

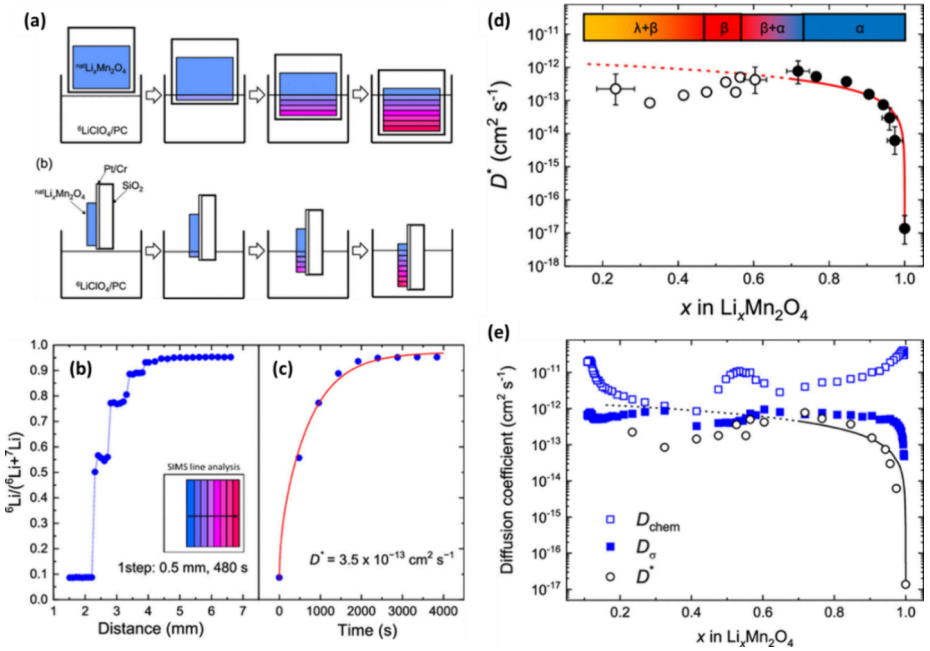

Figure 8. (a) Illustrates the stepwise ^{6}Li exchange method which enables room-temperature tracer diffusion analysis. Panels (b) and (c) present representative ^{6}Li isotope profiles for $Li_{0.6}Mn_2O_4$ and the corresponding extraction of the tracer diffusion coefficient (D^*). (d) Composition dependence of D^* and (e) compares D^* with chemical ($\tilde{D}$) and conductivity (D_σ) diffusion coefficients. Reproduced from ref 168. Copyright [2020] American Chemical Society.

defect-assisted pathways such as antiphase boundaries, coupled with rapid ab-plane transport between successive defects.[169]

Impact of Electrolyte Properties on Interfaces and Battery Performance

TFSSBs represent a distinct class of electrochemical energy-storage devices in which all battery components, cathode, SE, and anode, are fabricated as thin films, typically with thicknesses ranging from tens of nanometers to a few micrometers. TFSSBs offer intrinsic advantages over bulk solid-state and liquid-electrolyte batteries, including elimination of leakage and flammability risks, high interfacial stability, rapid charge−discharge capability, and compatibility with microelectronic integration. However, their development critically depends on SE materials selection, thin-film deposition fidelity, and interfacial engineering, as we discussed in the above sections. We have extensively worked on TFSSBs using PLD, and trace the evolution of TFSSB research, from early demonstrations of LiPON-based cells to high-rate oxide systems fabricated by PLD. The earliest demonstration of a PLD-enabled TFSSB was realized in a fully inorganic configuration, representing a landmark advance in thin-film battery research.[135] In that work, Kuwata et al. constructed a multilayer device consisting of a crystalline $LiCoO_2$ cathode, an amorphous $Li_2O-V_2O_5-SiO_2$ (LVSO) SE, and an amorphous SnO anode, with most layers deposited by PLD.[135]

A schematic of the device architecture is presented in Figure 9a, while the cross-sectional SEM micrograph in Figure 9b reveals compact and uniform $LiCoO_2$, LVSO, and SnO films separated by abrupt interfaces, with an overall thickness of roughly 2 μm. The deposited LVSO electrolyte layer exhibits a dense and smooth morphology which is free from pinholes. The compositional analysis indicates a stoichiometry of $Li_{2.2}V_{0.54}Si_{0.46}O_{3.4}$. Impedance spectroscopy measurements yielded an ionic conductivity of 2.5×10^{-7} S cm^{-1} at 25 °C with an activation energy of 0.54 eV. Further, the electrochemical testing of the PLD-grown TFSSB confirmed stable battery operation, as shown in Figures 9c and 4d. The TFSSBs reach an open-circuit voltage of approximately 2.7 V at full charge and maintain reversible charge−discharge behavior over 100 cycles within a 0−3.3 V window. Although the discharge capacity gradually declines to about 45% of its initial value after 100 cycles, the cell preserves high cycling efficiency.[135] Post-cycling cross-sectional analysis (Figure 9e) shows that both the LVSO electrolyte and the cathode/electrolyte and anode/electrolyte interfaces remain smooth and intact, underscoring the suitability of amorphous LVSO films and PLD processing for reliable thin-film microbattery fabrication.

Moreover, Kuwata et al. employed the high-rate PLD (Figure 10a) to fabricate TFSSBs, achieving deposition rates of approximately 2.2−3.4 μm h^{-1} for $LiCoO_2$, an order of magnitude higher than conventional PLD approaches through the use of high-repetition, high-power lasers.[86] When integrated with amorphous Li_3PO_4 SE into TFSSBs (cross-sectional SEM image shown in Figure 10b), the areal capacity[86] increased monotonically with cathode thickness, reaching a maximum value of ∼470 μAh cm^{-2}. They also optimized the synthesizes of high-quality Li_3PO_4 thin films by PLD as SE for TFSSBs, and their structural, compositional, ionic transport, and electrochemical properties were systematically evaluated. Using an ArF excimer laser, dense and smooth amorphous Li_3PO_4 films were obtained, which provides sufficiently high photon energy. The microscopy and XRD confirmed the uniform morphology and amorphous nature of the ArF-grown films.[45] The Li_3PO_4 electrolyte behaves as a single lithium-ion conductor with an ionic conductivity of

https://doi.org/10.1021/acsaelm.6c00171
ACS Appl. Electron. Mater. 2026, 8, 4855−4875

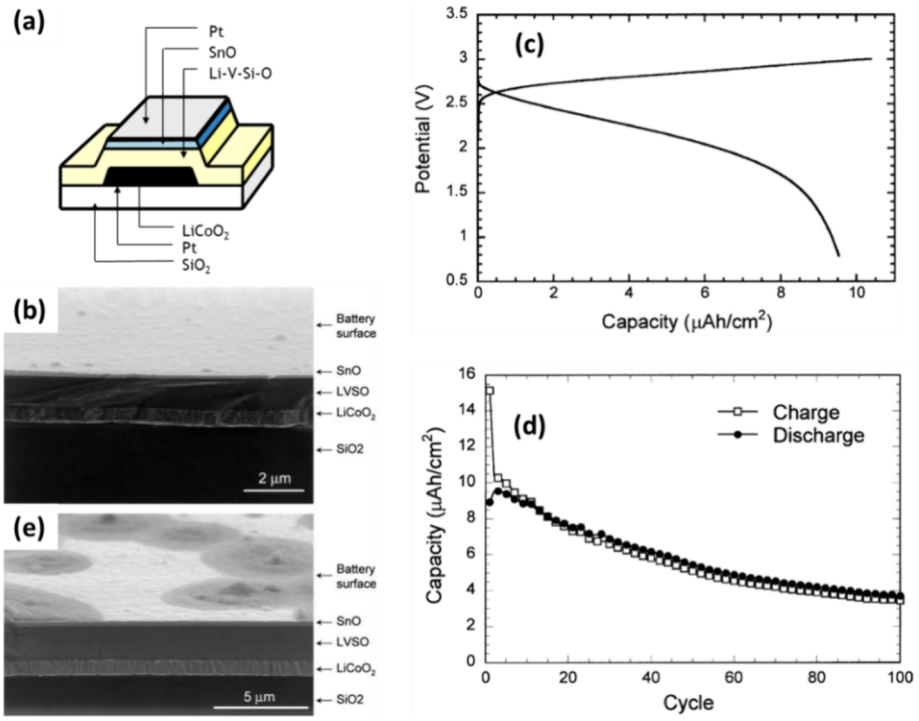

Figure 9. (a) Schematic illustration of an TFSSBs on a SiO_2 substrate. Cross-sectional SEM image of the (b) PLD-fabricated TFSSBs. (c) Initial charge−discharge voltage profiles of the thin-film battery measured under constant current conditions, demonstrating reversible lithium intercalation/deintercalation within the $LiCoO_2$ cathode. (d) Cycling performance of the thin-film battery, showing gradual capacity fading over 100 cycles. (e) Cross-sectional SEM image after prolonged charge−discharge cycling, confirming that the electrolyte layer and cathode−electrolyte interface remain intact without visible delamination or cracking. Reproduced or adapted with permission from ref 135. Copyright [2004] [Elsevier].

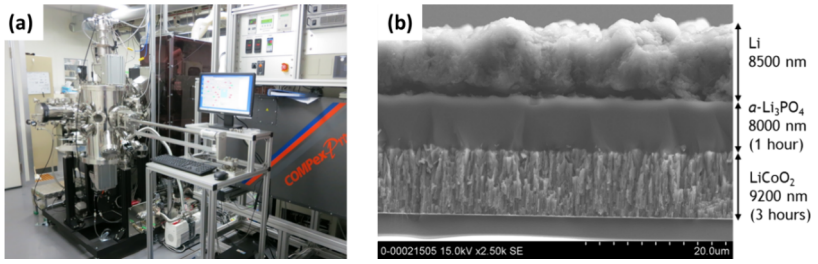

Figure 10. (a) Photograph of the high-rate PLD system, enabling deposition rates several times higher than conventional PLD processes. (b) Cross-sectional SEM image of a thick $LiCoO_2$ cathode film deposited by high-rate PLD, illustrating dense columnar microstructure. Reproduced or adapted with permission from ref 86. Copyright [2018] [Elsevier].

4.0×10^{-7} S cm^{-1} at 25 °C and an activation energy of 0.58 eV, while maintaining electrochemical stability over a wide potential window from 0 to 4.7 V vs Li/Li^+. Spectroscopic analysis revealed that the films consist of interconnected $(PO_4)^{3-}$ tetrahedra and $(P_2O_7)^{4-}$ units, and a decrease in ionic conductivity with increasing oxygen pressure during deposition was attributed to lithium loss.

Further, fully inorganic $Li/Li_3PO_4/LiCoO_2$ TFSSBs (schematic shown in Figure 11a) fabricated entirely by PLD demonstrated excellent lithium intercalation behavior and outstanding long-term stability between 3.0 and 4.4 V. Cyclic voltammetry performed at scan rates from 3 to 60 mV min^{-1} showed highly reversible electrochemical responses with sharp redox peaks between 3.7 and 4.4 V, corresponding to well-defined phase transitions within the layered $LiCoO_2$ structure, indicative of fast charge-transfer kinetics at the cathode−electrolyte interface, as shown in Figure 11b. Charge−discharge measurements revealed stable capacities with $LiCoO_2$ utilization as high as 95%, minimal polarization, and virtually no capacity fading even after 1000 cycles, with post-cycling profiles nearly identical to those of the initial cycles.[45] Compared with liquid-electrolyte systems, where electrolyte decomposition and cobalt dissolution severely limit cycling stability at high voltages, the solid-state configuration retained up to 99% of its initial capacity over prolonged cycling (Figure 11c), underscoring the critical role of Li_3PO_4 electrolytes in enhancing both the safety and lifetime of

https://doi.org/10.1021/acsaelm.6c00171
ACS Appl. Electron. Mater. 2026, 8, 4855−4875

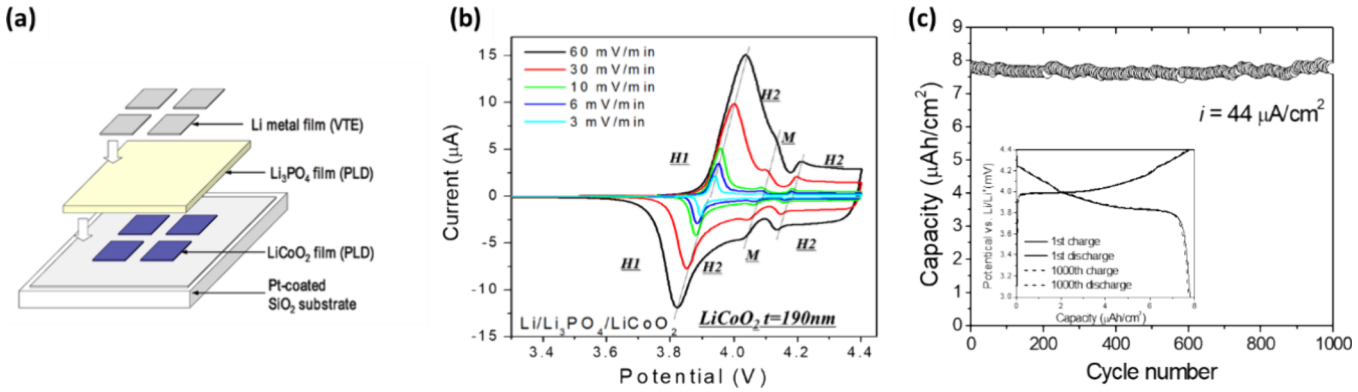

Figure 11. (a) Schematic illustration of TFSSBs Li/Li_3PO_4/$LiCoO_2$ fabricated on a Pt-coated SiO_2 glass substrate. (b) Cyclic voltammograms recorded at room temperature over scan rates ranging from 3 to 60 mV min^{-1}. (c) Cycling performance and representative charge−discharge profiles[45] measured between 3.0 and 4.4 V at a current density of 44 μA cm^{-2}. Reproduced or adapted with permission from ref 45. Copyright [2010] [Elsevier].

high-voltage lithium thin-film batteries. Thus, these PLD-based TFSSBs, clearly position Kuwata et al.'s contributions as foundational to the development of TFSSBs.[13,45,84,86−89,134,135,170] However, despite substantial progress, several fundamental challenges remain unresolved, which include the simultaneous realization of interfacial phenomena, the suppression of interfacial resistance to below 10 Ω cm^2, and the extension of thin film battery concepts beyond micro-power applications. Further progress in interface engineering and thin film processing is expected to address these challenges and expand the applicability of PLD-based TFSSBs.

Advanced Characterization of PLD-Grown SEs and TFSSBs

In PLD TFSEs, interfacial phenomena exert a first-order control over the electrochemical performance, rate capability, and long-term reliability of TFSSBs. Unlike solution-processed or sputtered architectures, PLD uniquely combines stoichiometric fidelity with subnanometer thickness control, which enables the fabrication of dense amorphous, nanocrystalline, and epitaxial electrolyte layers whose interfaces can be engineered and interrogated with exceptional precision. When coupled with fully in-vacuo (UHV-connected) processing, where cathode, electrolyte, and lithium anode are sequentially deposited without air exposure, PLD provides an ideal platform for isolating intrinsic interfacial transport, redox, and phase-transition mechanisms, free from parasitic surface contamination and adventitious interphases.[171] However, this same level of control renders PLD interfaces exquisitely sensitive to lithium chemical potential, plume− surface interactions, redox compatibility, and diffusion kinetics, as discussed above. As a result, interfacial stability in PLD-grown TFSEs, such as oxide, oxynitride, and phosphate electrolytes (Li_3PO_4, LiPON, LLZO, LATP/LAGP, and LISICON derivatives), has emerged as one of the most intensively scrutinized aspects of TFSSB design. At both cathode and anode interfaces, uncontrolled electronic leakage, interdiffusion, and SCL formation can degrade ionic conductivity, promote dendritic failure, or trigger chemically mixed interphases. Addressing these effects requires a combination of complementary characterization techniques, each probing distinct aspects of interfacial behavior, including structural evolution, chemical diffusion, and electronic reconstruction.

Operando Raman Spectroscopy. In situ micro-Raman spectroscopy directly probes local structural changes and phase transitions for directly visualizing structural and interfacial dynamics in PLD-fabricated TFSSBs. In a seminal study, Matsuda et al. employed in situ Raman spectroscopy to investigate PLD-grown $LiCoO_2$/Li_3PO_4 thin-film cells during electrochemical cycling.[172] By recording spectra from both the electrolyte-facing front surface and the Li-contact back surface through a transparent ITO current collector (Figure 12a,b), the authors achieved spatially resolved tracking of phase evolution in Li_xCoO_2 under operating conditions. Using in situ micro-Raman spectroscopy, they provided a clean view of structural evolution during electrochemical cycling to directly monitor the structural evolution of the Li_xCoO_2 cathode during electrochemical cycling.[172] The study focuses on tracking the A_{1g} and E_g Raman-active modes of $LiCoO_2$, which serve as sensitive probes of the changes in the *c*-axis lattice parameter associated with lithium deintercalation, as shown in Figure 12c,d (front surface) and Figure 12e,f (back surface).[172] During charging, both vibrational modes shift to lower wavenumbers as Li is extracted and the cathode undergoes the well-known sequence of phase transitions from H1 → H2 → monoclinic → H2′, with the largest shifts occurring around 3.9−4.1 V, where the two-phase coexistence begins. A key finding is that front-surface measurements show pronounced hysteresis in the Raman peak positions between charge and discharge, whereas back-surface measurements show almost no hysteresis. By correlating these results with the geometry of the cell, the authors show that the hysteresis arises from the diffusion-limited propagation of the H1/H2 phase boundary, such that at the front surface, the Raman probe is located ∼1 μm away from the Li contact, so structural changes lag behind the electrochemical state due to finite Li diffusion ($D \sim 1 \times 10^{-11}$ cm^2 s^{-1}), whereas beneath the Li anode the structural transformation is immediate. Moreover, a closely related operando Raman investigation by Kuwata et al. extended this framework to PLD-fabricated Li/a-Li_3PO_4/$LiMn_2O_4$ thin-film batteries.[13] Thin-film batteries with a Li/Li_3PO_4/$LiMn_2O_4$ configuration were fabricated by PLD and thermal evaporation, enabling optical access to the cathode during electrochemical operation. The in situ Raman spectra clearly resolved the characteristic vibrational fingerprints of the α ($LiMn_2O_4$), β ($Li_{0.5}Mn_2O_4$),

https://doi.org/10.1021/acsaelm.6c00171
ACS Appl. Electron. Mater. 2026, 8, 4855−4875

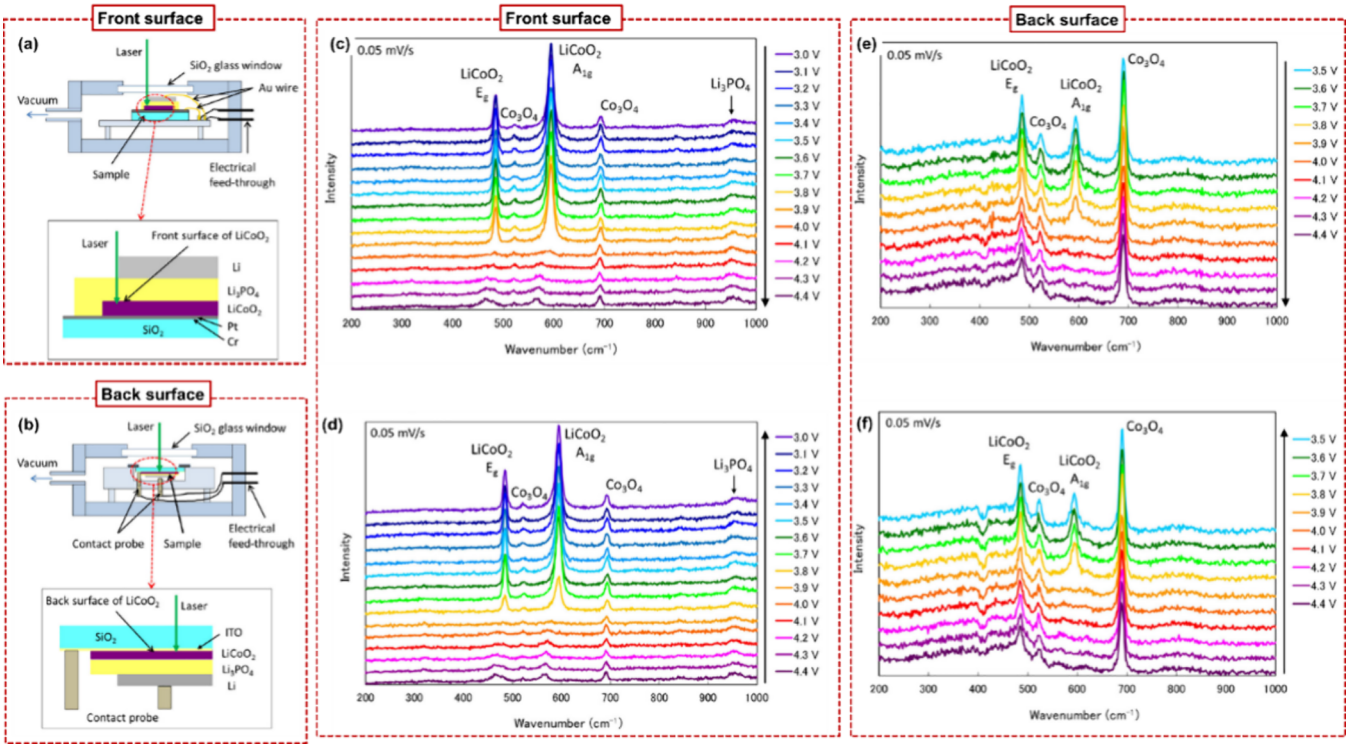

Figure 12. Schematic illustration of (a) the front side and (b) the back side of the TFSSBs, which are configured for in situ Raman measurements. The corresponding Raman spectra collected from the front-facing Li_xCoO_2 cathode are presented for (c) the charging step and (d) the discharge step and the back side of the TFSSBs for (e) charging and (f) discharging. Reproduced or adapted with permission from ref 172. Copyright [2019] [Elsevier].

and λ (MnO_2) phases, as the cathode underwent sequential α → β → λ phase transitions, while the reverse sequence occurred during discharge. The authors implemented a one-dimensional diffusion model that couple's lithium chemical diffusion with a lattice-gas–based potential–composition relationship. By fitting the experimentally observed Raman hysteresis, an average chemical diffusion coefficient of Li^+ in $Li_xMn_2O_4$ of $\sim 6 \times 10^{-11}$ cm^2 s^{-1} was extracted. This value agrees well with diffusion coefficients previously determined for $LiMn_2O_4$ thin films using electrochemical and isotope tracer methods, reinforcing the physical validity of the model. Taken together, these studies demonstrate that the in situ Raman spectroscopy provides a uniquely powerful framework for elucidating diffusion-limited phase-transition dynamics and interfacial effects in TFSSBs.

XPS and UHV Processing. Haruta et al. reported a fully UHV-connected fabrication and characterization platform which integrates PLD, RF sputtering, and a thermal evaporation system in order to assemble TFSSBs entirely without air exposure.[171] The TFSSBs comprise PLD deposited $LiCoO_2$, sputtered LiPON, and thermally evaporated lithium. The fabricated TFSSBs show exceptionally sharp redox features with stable cycling even at rates up to 20 C. The structural analysis revealed that Li-ion transport proceeds preferentially along $LiCoO_2$ grain boundaries rather than across basal planes, while XPS confirmed the chemical stability of both Co and nitrogen environments in LiPON. Thus, Haruta et al. established a benchmark for probing intrinsic electrolyte/electrode interactions, which demonstrates that UHV-prepared interfaces can sustain high-rate operation without post-annealing. Further, the interfacial degradation in layered oxide cathodes can be mitigated through conformal surface coatings. Kato et al. systematically compared amorphous lithium tantalate (LTaO) and lithium niobate (LNbO) coatings deposited by PLD on $LiCoO_2$ thin films.[173] SIMS-based $^6Li/^7Li$ isotope exchange revealed lithium tracer diffusion coefficients of $\sim 10^{-13}$ cm^2 s^{-1} in both coatings, among the highest reported for amorphous lithium oxides. While both coatings reduced charge-transfer resistance and improved high-rate performance, XPS revealed partial oxidative degradation of LTaO during cycling, whereas LNbO remained chemically stable. These results demonstrate that high lithium mobility alone is insufficient; long-term interfacial performance is governed by the balance between fast ion transport and chemical robustness.[173] Hence, X-ray-based methods are particularly powerful for elucidating redox heterogeneity, degradation pathways, and chemo-mechanical coupling at interfaces.

X-ray Microscopy and X-ray Absorption. Researchers have investigated a thin-film battery using operando full-field transmission X-ray microscopy and operando hard X-ray photoelectronspectroscopy (HAXPES). Ishiguro et al. employed operando full-field transmission X-ray microscopy combined with X-ray absorption fine structure spectroscopy to visualize chemical-state evolution in $LiCoO_2$ cathodes and $Fe_2(MoO_4)_3$ anodes in TFSSBs.[174] It revealed pronounced cycling-induced degradation and distinct redox-percolation behaviors such as the $LiCoO_2$ exhibited interfacial exfoliation with Co oxidation. While $Fe_2(MoO_4)_3$ partially decomposed into γ-Fe_2O_3 with extensive cracking, which underscores the importance of interface and phase-stability engineering. While, Hikima et al. introduced HAXPES as a transformative probe of buried electronic structures in TFSSBs.[175] In $Al/Li_{2-x}MnO_3$/

https://doi.org/10.1021/acsaelm.6c00171
ACS Appl. Electron. Mater. 2026, 8, 4855−4875

LASGTP/Li_3PO_4/Li cells, HAXPES revealed substantial Fermi-level shifts, an n-type to p-type transition during delithiation, and strong interfacial band bending at high states of charge. These electronic reconstructions lead to charge accumulation and capacitor-like behavior, kinetically suppressing further lithium extraction despite increasing applied bias. The findings demonstrate that TFSSB performance is governed not only by ionic transport but also by interfacial electronic structure and space-charge effects, a dimension inaccessible to purely structural probes.[175] Thus, HAXPES can provide direct access to buried electronic structures and band alignment at interfaces. Unlike conventional XPS, HAXPES probes deeper into multilayer stacks.

Neutron Depth Profiling. At cathode−electrolyte interfaces, Shimizu et al. provided a mechanistic explanation for the remarkable stability of high-voltage LNMO/LiPON interfaces using neutron depth profiling (NDP), first-principles calculations, and cryogenic electron microscopy.[12] NDP revealed localized lithium enrichment (∼3%) at the interface, which is arising from chemical overlithiation of LNMO during LiPON deposition. While DFT showed that excess lithium is accommodated via $Mn^{4+} \rightarrow Mn^{3+}$ reduction and Jahn−Teller distortion, forming a chemically benign, ion-conductive interphase that suppresses degradation over >600 cycles. Thus, NDP enables quantitative, depth-resolved measurement of lithium concentration across buried interfaces, providing direct insight into lithium redistribution and interfacial accumulation. It is particularly powerful for correlating lithium transport and interphase formation with electrochemical stability in TFSSBs.

STEM−EELS. The STEM−EELS enables quantitative mapping of Li distribution and electronic structure with subnanometer resolution.[16−20] Such as the work by Nomura et al. represents a milestone in quantitative operando STEM−EELS for SSBs.[16] This study employs a model TFSSB architecture consisting of a $LiCoO_2$ thin-film cathode integrated with SEs, where the cathode layer is fabricated via PLD to achieve dense, epitaxial-quality films with well-defined interfaces. By combining hyperspectral EELS imaging with non-negative matrix factorization (NMF), they achieved spatially resolved Li concentration mapping during electrochemical cycling. The study reveals that lithiation/delithiation in $LiCoO_2$ cathodes proceeds in a markedly nonuniform manner, which differs from the conventional assumption of homogeneous Li extraction and insertion. Spatially resolved measurements identify the formation of an ∼10 to 20 nm thick interfacial region at the CEI that remains electrochemically inactive, which is found to be a heterogeneous mixture of $LiCoO_2$ and Co_3O_4 phases. This acts as a kinetic bottleneck to ion transport, as it lacks viable Li diffusion pathways. It provides direct experimental evidence that interfacial resistance originates from structurally disordered regions. While the local chemical heterogeneity governs Li transport across interfaces rather than bulk ionic conductivity alone. Moreover, a direct correlation between ionic distribution and electronic structure evolution can be easily probed by EELS, as it has the capability of detecting the Li K-edge and transition metal $L_{2,3}$ edges. In particular, localized Li depletion and electronic inactivity are found to be due to suppressed redox activity, which results from the oxidation of Co^{3+} to Co^{4+}. Thus, the unique strength of STEM−EELS by integrated mapping of ionic and electronic states helps resolve coupled transport phenomena at buried solid−solid interfaces.

Cryo-TEM. By suppressing radiolysis and thermally activated diffusion, the cryo-TEM preserves metastable and beam-sensitive interphases.[176−179] When it combines with EELS, it can enable unprecedented insight into metastable interphases and Li transport pathways at solid−solid interfaces by preserving their native chemical and structural states.[14,15] Cheng et al.[15] analyzed the Li/LiPON interfaces via cryo-TEM and revealed the formation of an approximately 76 nm thick interphase exhibiting pronounced compositional gradients. It is found to be a mosaic-like nanostructure which comprises Li_2O, Li_3N, and Li_3PO_4 domains embedded within an amorphous matrix. The interphase is intrinsically heterogeneous rather than a uniform layer as often assumed in continuum descriptions.[15] While comparing it with the theoretical analysis, Cheng et al.[15] showed that interstitial diffusion barriers for decomposition species vary significantly (e.g., ∼0.42 eV for P, ∼0.5 eV for O, and ∼1.08 eV for N), which implies that mobile species such as P and N can drive chemical redistribution and sustain dynamic interphase evolution. This supports a diffusion-mediated growth mechanism of the interphase rather than a purely reaction-limited process. Furthermore, cryo-EELS facilitates the detection of light elements such as Li, N, and O with minimized beam-induced damage, which enables spatial mapping of chemical gradients across buried interfaces and provides a coupled chemo-mechanical perspective of interphase formation. Extending this approach to cathode−electrolyte systems, cryo-TEM studies of LNMO/LiPON interfaces were carried out by Shimizu et al., where the LNMO cathode is grown using PLD to ensure phase purity and controlled crystallinity.[12] The optimized deposition results in the formation of stable and coherent interfaces. The cryo-TEM analysis reveals structurally coherent and stable interfaces regions with minimal morphological evolution upon cycling, where only localized nanocrystalline decomposition products such as Li_3PO_4 and Li_2PO_2N are observed. In contrast to layered oxides like $LiCoO_2$, the spinel framework of LNMO accommodates Li insertion/extraction with reduced structural perturbation, thereby results in enhanced interfacial stability. Additionally, Li accumulation at $LiCoO_2$/LiPON interfaces was linked to disorder-induced phase formation, which confirms that the interface stability is strongly dependent on cathode crystal structure. Thus, cryo-TEM preserves highly reactive solid−solid interfaces in their native state by suppressing beam-induced damage and thermally activated diffusion, which enables direct visualization of metastable interphases and nanoscale structural heterogeneity. In contrast, STEM−EELS provides spatially resolved, quantitative mapping of Li distribution and transition-metal electronic states, allowing direct correlation between ionic transport and local redox activity at buried interfaces.

■ OUTLOOK AND FUTURE RESEARCH DIRECTIONS

Although substantial progress has been achieved in the synthesis and integration of TFSEs, a critical bottleneck persists in the quantitative understanding of lithium diffusion within ultrathin SE with deposition parameters as well as in TFSSBs. The advancement of materials processing strategies and operando characterization methodologies to address the complexed interface-dominated nature of ion transport in TFSEs and TFSSBs is quite important. Techniques such as PLD offer exceptional control over film stoichiometry, density, and microstructure. However, the direct influence of deposition

https://doi.org/10.1021/acsaelm.6c00171
ACS Appl. Electron. Mater. 2026, 8, 4855−4875

parameters (laser fluence, substrate temperature, background pressure, and target−substrate distance) on ionic transport properties and diffusion kinetics remains insufficiently quantified. Future efforts must therefore focus on establishing explicit correlations between growth conditions and transport parameters through combined experimental and computational studies, including density functional theory and kinetic modeling to elucidate defect formation and migration mechanisms under nonequilibrium growth conditions.

In contrast to bulk systems as well as thin-film electrodes (cathodes), where isotope-exchange techniques along with tracer diffusion measurements are relatively well used,[133,169,180−185] TFSEs remain underexplored, especially with respect to isotope-resolved TOF-SIMS analysis. The limited investigation in this direction hinders further growth of TFSEs as it is highly important to realize the modified diffusion pathways, migration barriers, and even transport mechanisms compared to their bulk counterparts. These properties are quite different from their bulk because reduced dimensionality results in different defect chemistry, and strong interfacial electric fields, which are further affected by the substrate-induced strains. Thus, such studies help explicitly distinguish between bulk, grain-boundary, and interface-mediated transport contributions. While the development of correlative and multimodal characterization frameworks is essential, too, wherein TOF-SIMS measurements are directly coupled with high-resolution structural and spectroscopic probes, including STEM−EELS, XRD, Raman, and electrochemical impedance spectroscopy. Hence in all, this integrated approach will enable the establishment of rigorous structure−transport relationships by directly correlating local chemical environments, defect distributions, and interphase compositions with measured diffusion profiles. Without these quantitative and spatially resolved insights, current approaches to TFSEs design and optimization remain largely empirical and lack predictive capability.

Furthermore, in case of TFSSBs, operando studies remain limited, where maintaining stable analysis conditions under applied bias and nanoscale geometries presents significant experimental challenge. As a result, direct observation of dynamic lithium redistribution and interfacial evolution during cycling is still not well-documented in literature. Given that interfaces in TFSSBs often dominate overall ionic resistance due to the high surface-to-volume ratio, there is a need to probe lithium diffusion across buried interfaces, such as electrolyte/electrode and electrolyte/current collector junctions. At these locations, the transport behavior is highly influenced by interphase formation, space-charge layers (SCLs), and strain gradients. Thus, there is need to use of advanced experimental approaches that can quantitatively visualize the ion dynamics in TFSEs as well as in TFSSBs during operando or even quasi-operando conditions. While there are few reports on visualization of ion dynamics in cathodes, there is only limited literature available on TFSEs. Moreover, this area remains not well-documented in literature for TFSSBs, too, which is essential to know the transport pathways and their dynamically evolution with cycling-induced structural and chemical transformations at interfaces. The direct observation of dynamic lithium redistribution and interfacial evolution during cycling is essential to further optimized the TFSSBs. One of the ways to investigate the dynamically evolution is the use of operando TOF-SIMS. While the operando SIMS studies remain limited, too, where maintaining stable analysis conditions under applied bias and nanoscale geometries presents significant experimental challenge. For achieving a predictive understanding of ion transport in TFSEs and accelerating the rational design and deployment of next-generation TFSSBs, there is high need to address these interconnected challenges through coordinated experimental and theoretical efforts.

CONCLUSIONS

In advancing next-generation solid-state microbatteries, TFSEs play a central role, where ionic transport, interphase evolution, and mechanical stability are governed not only by intrinsic bulk properties, but predominantly by nanoscale confinement effects and deposition-induced microstructural features. These characteristics ultimately determine the overall ion transport behavior in SEs. Among the available deposition techniques, PLD provides a particularly powerful route for TFSE fabrication, as it enables precise control over stoichiometry, defect chemistry, and film density, thereby stabilizing metastable and nonequilibrium phases that are inaccessible through conventional synthesis methods. In addition, PLD helps tailor ion transport pathways and minimize interfacial resistance, as it can engineer atomically sharp and chemically well-defined interfaces. These attributes collectively position PLD not merely as a fabrication tool, but as a deterministic approach for tuning structure−property relationships in TFSEs, thus directly influencing ionic conductivity and device-level performance. Concurrently, a critical gap persists within the deposited TFSE. While the TOF-SIMS technique coupled with isotope-exchange has been widely used for cathodes, there is limited literature on quantitative evaluation of lithium diffusion in TFSEs, which is necessary to optimize the TFSSBs. Addressing this limitation is essential for establishing reliable correlations between PLD growth parameters, microstructural features, and ion transport properties. It is important to highlight here that the operando studies on TFSSBs, which result in direct observation of dynamic lithium redistribution and interfacial evolution during cycling, remain limited, too. There are significant experimental challenges to maintain stable analysis conditions under applied bias and nanoscale geometries. Thus, the future progress will therefore depend on systematic, and quantitatively rigorous studies that leverage PLD's tunability to decouple bulk and interfacial contributions to diffusion. It will enable a more predictive design paradigm along with the development of multimodal characterizations which can probe the in situ ion behavior in TFSSBs. In this context, PLD-grown thin films will continue to serve as both functional components and model systems, which reinforce their central role in advancing the fundamental understanding and technological development of SSB systems.

AUTHOR INFORMATION

Corresponding Author

Naoaki Kuwata − *Research Center for Energy and Environmental Materials, National Institute for Materials Science (NIMS), Tsukuba, Ibaraki 305 0044, Japan; Graduate School of Chemical Sciences and Engineering, Hokkaido University, Sapporo, Hokkaido 060-8628, Japan;* orcid.org/0000-0002-0736-6967; Email: KUWATA.Naoaki@nims.go.jp

https://doi.org/10.1021/acsaelm.6c00171
ACS Appl. Electron. Mater. 2026, 8, 4855−4875

Authors

Prince Sharma – *Research Center for Energy and Environmental Materials, National Institute for Materials Science (NIMS), Tsukuba, Ibaraki 305 0044, Japan*

Gen Hasegawa – *Research Center for Energy and Environmental Materials, National Institute for Materials Science (NIMS), Tsukuba, Ibaraki 305 0044, Japan*; orcid.org/0000-0002-9297-6902

Sihao Xing – *Research Center for Energy and Environmental Materials, National Institute for Materials Science (NIMS), Tsukuba, Ibaraki 305 0044, Japan; Graduate School of Chemical Sciences and Engineering, Hokkaido University, Sapporo, Hokkaido 060-8628, Japan*

Complete contact information is available at: https://pubs.acs.org/doi/10.1021/acsaelm.6c00171

Funding

The work was supported by the Japan Society for the Promotion of Science [P24365].

Notes

The authors declare no competing financial interest.

■ ACKNOWLEDGMENTS

This work was supported by the Japan Society for the Promotion of Science (JSPS) through a Postdoctoral Fellowship [P24365], funded by the Ministry of Education, Culture, Sports, Science and Technology (MEXT), Japan. This study is also supported by JSPS KAKENHI grant numbers 24KF027 and 24H02205, and JST COI-NEXT "Center for Advanced Battery Collaboration" grant number JPMJPF2016.

■ REFERENCES

(1) Nathan, M. Microbattery Technologies for Miniaturized Implantable Medical Devices. *Curr. Pharm. Biotechnol.* **2010**, *11* (4), 404–410.

(2) Dudney, N. J. Thin Film Micro-Batteries. *Electrochem. Soc. Interface* **2008**, *17* (3), No. 44.

(3) Torres, E. O.; Rincón-Mora, G. A. Electrostatic Energy-Harvesting and Battery-Charging CMOS System Prototype. *IEEE Trans. Circuits Syst. I Regul. Pap.* **2009**, *56* (9), 1938–1948.

(4) Bock, D. C.; Marschilok, A. C.; Takeuchi, K. J.; Takeuchi, E. S. Batteries Used to Power Implantable Biomedical Devices. *Electrochim. Acta* **2012**, *84*, 155–164.

(5) Dudney, N. J.; Neudecker, B. J. Solid State Thin-Film Lithium Battery Systems. *Curr. Opin. Solid State Mater. Sci.* **1999**, *4* (5), 479–482.

(6) Futscher, M. H.; Brinkman, L.; Müller, A.; Casella, J.; Aribia, A.; Romanyuk, Y. E. Monolithically-Stacked Thin-Film Solid-State Batteries. *Commun. Chem.* **2023**, *6* (1), 110.

(7) Tarascon, J. M.; Armand, M. Issues and Challenges Facing Rechargeable Lithium Batteries. In *Materials for Sustainable Energy*; World Scientific, **2010**; Vol. 414; pp 171−179.

(8) Yu, X.; Bates, J. B.; Jellison, G. E.; Hart, F. X. A Stable Thin-Film Lithium Electrolyte: Lithium Phosphorus Oxynitride. *J. Electrochem. Soc.* **1997**, *144* (2), 524–532.

(9) Liang X. P.; Tan, F. H.; Wei, F.; Du, J. Research Progress of All Solid-State Thin Film Lithium Battery *IOP Conf. Ser.: Earth Environ. Sci.* **2019** *218* No. 012138.

(10) Madinabeitia, I.; Rikarte, J.; Etxebarria, A.; Baraldi, G.; Jos, F.; Garbayo, I.; Garc, A.; Miguel, A. Monolithic All-Solid-State High-Voltage Li-Metal Thin-Film Rechargeable Battery. *ACS Appl. Energy Mater.* **2022**, *5*, 12120.

(11) Jones, S. D.; Akridge, J R; Shokoohi, F. K. Thin Film Rechargeable Li Batteries. *Solid State Ion.* **1994**, *69* (3−4), 357–368.

(12) Shimizu, R.; Cheng, D.; Weaver, J. L.; Zhang, M.; Lu, B.; Wynn, T. A.; Burger, R.; Kim, M.; Zhu, G.; Meng, Y. S. Unraveling the Stable Cathode Electrolyte Interface in All Solid-state Thin-film Battery Operating at 5 V. *Adv. Energy Mater.* **2022**, *12* (31), No. 2201119.

(13) Kuwata, N.; Matsuda, Y.; Okawa, T.; Hasegawa, G.; Kamishima, O.; Kawamura, J. Ion Dynamics of the $Li_xMn_2O_4$ Cathode in Thin-Film Solid-State Batteries Revealed by in Situ Raman Spectroscopy. *Solid State Ion.* **2022**, *380*, No. 115925.

(14) Lin, R.; He, Y.; Wang, C.; Zou, P.; Hu, E.; Yang, X.-Q.; Xu, K.; Xin, H. L. Characterization of the Structure and Chemistry of the Solid−Electrolyte Interface by Cryo-EM Leads to High-Performance Solid-State Li-Metal Batteries. *Nat. Nanotechnol.* **2022**, *17* (7), 768–776.

(15) Cheng, D.; Wynn, T. A.; Wang, X.; Wang, S.; Zhang, M.; Shimizu, R.; Bai, S.; Nguyen, H.; Fang, C.; Kim, M. Unveiling the Stable Nature of the Solid Electrolyte Interphase between Lithium Metal and LiPON via Cryogenic Electron Microscopy. *Joule* **2020**, *4* (11), 2484–2500.

(16) Nomura, Y.; Yamamoto, K.; Hirayama, T.; Ohkawa, M.; Igaki, E.; Hojo, N.; Saitoh, K. Quantitative Operando Visualization of Electrochemical Reactions and Li Ions in All-Solid-State Batteries by STEM-EELS with Hyperspectral Image Analyses. *Nano Lett.* **2018**, *18* (9), 5892–5898.

(17) Cho, B.-K.; Jung, S.-Y.; Park, S.-J.; Hyun, J.-H.; Yu, S.-H. In Situ/Operando Imaging Techniques for next-Generation Battery Analysis. *ACS Energy Lett.* **2024**, *9* (8), 4068–4092.

(18) Sun, Z.; Pan, J.; Chen, W.; Chen, H.; Zhou, S.; Wu, X.; Wang, Y.; Kim, K.; Li, J.; Liu, H. Electrochemical Processes and Reactions in Rechargeable Battery Materials Revealed via in Situ Transmission Electron Microscopy. *Adv. Energy Mater.* **2024**, *14* (2), No. 2303165.

(19) Cheng, D.; Hong, J.; Lee, D.; Lee, S.-Y.; Zheng, H. In Situ TEM Characterization of Battery Materials. *Chem. Rev.* **2025**, *125* (4), 1840–1896.

(20) Alsaç, E. P.; Nelson, D. L.; Yoon, S. G.; Cavallaro, K. A.; Wang, C.; Sandoval, S. E.; Eze, U. D.; Jeong, W. J.; McDowell, M. T. Characterizing Electrode Materials and Interfaces in Solid-State Batteries. *Chem. Rev.* **2025**, *125* (4), 2009–2119.

(21) Sharma, P.; Hasegawa, G.; Xing, S.; Kuwata, N. Unlocking the Potential of Battery Technologies through Time-of-Flight Secondary Ion Mass Spectrometry. *Sci. Technol. Adv. Mater.* **2025**, *26* (1), No. 2580917.

(22) Ohnishi, T.; Takada, K. Synthesis and Orientation Control of Li-Ion Conducting Epitaxial $Li_{0.33}La_{0.56}TiO_3$ Solid Electrolyte Thin Films by Pulsed Laser Deposition. *Solid State Ionics* **2012**, *228*, 80–82.

(23) Fenech, M.; Sharma, N. Pulsed Laser Deposition-based Thin Film Microbatteries. *Chem. Asian J.* **2020**, *15* (12), 1829–1847.

(24) Kanazawa, S.; Baba, T.; Yoneda, K.; Mizuhata, M.; Kanno, I. Deposition and Performance of All Solid-State Thin-Film Lithium-Ion Batteries Composed of Amorphous Si/LiPON/VO-LiPO Multilayers. *Thin Solid Films* **2020**, *697*, No. 137840.

(25) Choolaei, M.; Vostakola, M. F.; Horri, B. A. Recent Advances and Challenges in Thin-Film Fabrication Techniques for Low-Temperature Solid Oxide Fuel Cells. *Crystals* **2023**, *13* (7), No. 1008.

(26) Park, M.; Zhang, X.; Chung, M.; Less, G. B.; Sastry, A. M. A Review of Conduction Phenomena in Li-Ion Batteries. *J. Power Sources* **2010**, *195* (24), 7904–7929.

(27) Sun, C.; Liu, J.; Gong, Y.; Wilkinson, D. P.; Zhang, J. Recent Advances in All-Solid-State Rechargeable Lithium Batteries. *Nano Energy* **2017**, *33*, 363–386.

(28) Patil, A.; Patil, V.; Shin, D. W.; Choi, J. W.; Paik, D. S.; Yoon, S. J. Issue and Challenges Facing Rechargeable Thin Film Lithium Batteries. *Mater. Res. Bull.* **2008**, *43* (8−9), 1913–1942.

(29) Alvarez-Fernandez, A.; Hernández, G.; Maiz, J. Unlocking Solid Polymer Electrolytes: Advancing Materials through Characterization-Driven Insights. *JACS Au* **2025**, *5* (8), 3701–3715.

(30) Jaugstetter, M.; Blanc, N.; Kratz, M.; Tschulik, K. Electrochemistry under Confinement. *Chem. Soc. Rev.* **2022**, *51* (7), 2491–2543.
(31) Li, G. Regulating Mass Transport Behavior for High-performance Lithium Metal Batteries and Fast-charging Lithium-ion Batteries. *Adv. Energy Mater.* **2021**, *11* (7), No. 2002891.
(32) Wang, J.; Li, L.; Hu, H.; Hu, H.; Guan, Q.; Huang, M.; Jia, L.; Adenusi, H.; Tian, K. V.; Zhang, J. Toward Dendrite-Free Metallic Lithium Anodes: From Structural Design to Optimal Electrochemical Diffusion Kinetics. *ACS Nano* **2022**, *16* (11), 17729–17760.
(33) Gao, H.; Wu, Q.; Hu, Y.; Zheng, J. P.; Amine, K.; Chen, Z. Revealing the Rate-Limiting Li-Ion Diffusion Pathway in Ultrathick Electrodes for Li-Ion Batteries. *J. Phys. Chem. Lett.* **2018**, *9* (17), 5100–5104.
(34) Madadi, M.; Heikkinen, M.; Philip, A.; Karppinen, M. Conformal High-Aspect-Ratio Solid Electrolyte Thin Films for Li-Ion Batteries by Atomic Layer Deposition. *ACS Appl. Electron. Mater.* **2024**, *6* (3), 1574–1580.
(35) Madadi, M.; Heikkinen, M.; Philip, A.; Karppinen, M. Highly Conformal Solid Electrolyte for Li-Ion Batteries By Atomic Layer Deposition. In *Electrochemical Society Meeting Abstracts 244*; The Electrochemical Society, Inc., **2023**; p 3396.
(36) Le Cras, F.; Berthou, W.; Legallais, M.; Landry, A.-K.; Nuernberg, R. B.; Pecquenard, B. Development of Thin Film Solid Electrolytes: From Conventional Approaches to High-Throughput Experimentation. In *MATSUS Spring 2025-Materials for Sustainable Development Conference*, **2025**.
(37) Neudecker, B. J.; Dudney, N. J.; Bates, J. B. " Lithium-Free" Thin-Film Battery with In Situ Plated Li Anode. *J. Electrochem. Soc.* **2000**, *147* (2), 517.
(38) Tian, B.; ⊠wiatowska, J.; Maurice, V.; Zanna, S.; Seyeux, A.; Marcus, P. Binary Iron-Chromium Oxide as Negative Electrode for Lithium-Ion Micro-Batteries - Spectroscopic and Microscopic Characterization. *Appl. Surf. Sci.* **2015**, *353*, 1170–1178.
(39) Walia, S.; Shah, C. M.; Gutruf, P.; Nili, H.; Chowdhury, D. R.; Withayachumnankul, W.; Bhaskaran, M.; Sriram, S. Flexible Metasurfaces and Metamaterials: A Review of Materials and Fabrication Processes at Micro- and Nano-Scales. *Appl. Phys. Rev.* **2015**, *2* (1), 11303.
(40) Yufit, V.; Golodnitsky, D.; Burstein, L.; Nathan, M.; Peled, E. X-Ray Photoelectron Spectroscopy and Time-of-Flight Secondary Ion Mass Spectroscopy Studies of Electrodeposited Molybdenum Oxysulfide Cathodes for Lithium and Lithium-Ion Microbatteries. *J. Solid State Electrochem.* **2008**, *12* (3), 273–285.
(41) Lacivita, V.; Artrith, N.; Ceder, G. Structural and Compositional Factors That Control the Li-Ion Conductivity in LiPON Electrolytes. *Chem. Mater.* **2018**, *30* (20), 7077–7090.
(42) Balaish, M.; Kim, K. J.; Chu, H.; Zhu, Y.; Gonzalez-Rosillo, J. C.; Kong, L.; Paik, H.; Weinmann, S.; Hood, Z. D.; Hinricher, J.; Miara, L. J.; Rupp, J. L. M. Emerging Processing Guidelines for Solid Electrolytes in the Era of Oxide-Based Solid-State Batteries. *Chem. Soc. Rev.* **2025**, *54* (19), 8925–9007.
(43) Liu, H.; Zhao, L.; Ye, Y.; Yang, X.; Zhang, Y.; Li, Q.; Li, R.; Liu, H.; Huang, B.; Wu, F.; Chen, R.; Li, L. Extremely Fast-Charging Batteries: Principle, Strategies, Detection, and Prediction. *Chem. Rev.* **2025**, *125* (20), 9553–9678.
(44) Chen, L.; Li, F.; Wang, F.; Bai, Z.; Zhang, Y.; Tang, Y. Decoding Hard Carbon Microstructure for Fast-Charging Lithium-Ion Batteries. *Adv. Funct. Mater.* **2025**, *36* No. e19895.
(45) Kuwata, N.; Iwagami, N.; Tanji, Y.; Matsuda, Y.; Kawamura, J. Characterization of Thin-Film Lithium Batteries with Stable Thin-Film Li_3PO_4 Solid Electrolytes Fabricated by ArF Excimer Laser Deposition. *J. Electrochem. Soc.* **2010**, *157* (4), A521.
(46) Ohnishi, T. Fabrication of Thin-Film Batteries Composed of $LiCoO_2$, Li_3PO_4, and Li Layers. *J. Solid State Electrochem.* **2024**, *28* (12), 4355–4366.
(47) Ohnishi, T.; Takada, K. Sputter-Deposited Amorphous Li_3PO_4 Solid Electrolyte Films. *ACS Omega* **2022**, *7* (24), 21199–21206.
(48) Cai, X.; Bao, W.; Zhao, L.; Zuo, Y.; Zhao, H.; Su, L.; Zhang, Y.; Zhang, H.; Xie, J. Investigation of Electrochemical Stability of ALD Grown Li_3PO_4 Thin Films and Its Application in High-Voltage PEO-based All-Solid-State Lithium Batteries. *Adv. Sustain. Syst.* **2025**, *9* (7), No. 2300392.
(49) Xu, H.; Yang, S.; Li, B. Pressure Effects and Countermeasures in Solid-State Batteries: A Comprehensive Review. *Adv. Energy Mater.* **2024**, *14* (16), No. 2303539.
(50) Sun, T.; Liang, Q.; Wang, S.; Liao, J. Insight into Dendrites Issue in All Solid-State Batteries with Inorganic Electrolyte: Mechanism, Detection and Suppression Strategies. *Small* **2024**, *20* (17), No. 2308297.
(51) Wolfenstine, J.; Allen, J. L.; Sakamoto, J.; Siegel, D. J.; Choe, H. Mechanical Behavior of Li-Ion-Conducting Crystalline Oxide-Based Solid Electrolytes: A Brief Review. *Ionics (Kiel).* **2018**, *24* (5), 1271–1276.
(52) Athanasiou, C. E.; Jin, M. Y.; Ramirez, C.; Padture, N. P.; Sheldon, B. W. High-Toughness Inorganic Solid Electrolytes via the Use of Reduced Graphene Oxide. *Matter* **2020**, *3* (1), 212–229.
(53) Hao, S.; Zhang, Q.; Kong, X.; Wang, Z.; Gao, X.; Shearing, P. R. Intrinsic Mechanical Parameters and Their Characterization in Solid-State Lithium Batteries. *Adv. Energy Mater.* **2025**, *15* (11), No. 2404384.
(54) Ayalew, K. H.; Palaniyandy, N.; Mathe, M. K.; Msomi, P. F. Garnet-Type LLZO Electrolytes for Solid-State Lithium Batteries: Interfaces, Conductivity, in-Situ Processing, and Industrial Prospects. *Chem. Eng. J.* **2025**, *524*, No. 168098.
(55) Machín, A.; Morant, C.; Márquez, F. Advancements and Challenges in Solid-State Battery Technology: An in-Depth Review of Solid Electrolytes and Anode Innovations. *Batteries* **2024**, *10* (1), 29.
(56) Thomas, F.; Mahdi, L.; Lemaire, J.; Santos, D. M. F. Technological Advances and Market Developments of Solid-State Batteries: A Review. *Materials (Basel).* **2024**, *17* (1), 239.
(57) Pearse, A. J.; Schmitt, T. E.; Fuller, E. J.; El-Gabaly, F.; Lin, C.-F.; Gerasopoulos, K.; Kozen, A. C.; Talin, A. A.; Rubloff, G.; Gregorczyk, K. E. Nanoscale Solid State Batteries Enabled by Thermal Atomic Layer Deposition of a Lithium Polyphosphazene Solid State Electrolyte. *Chem. Mater.* **2017**, *29* (8), 3740–3753.
(58) Mittal, M.; Sardar, S.; Jana, A.Nanofabrication Techniques for Semiconductor Chemical Sensors. In *Handbook of Nanomaterials for Sensing Applications*; Elsevier, **2021**; pp 119–137.
(59) Zhang, X.; Lok, M.; Tong, T.; Lee, S. K.; Reagen, B.; Chaput, S.; Duhamel, P. E. J.; Wood, R. J.; Brooks, D.; Wei, G. Y. A Fully Integrated Battery-Powered System-on-Chip in 40-Nm CMOS for Closed-Loop Control of Insect-Scale Pico-Aerial Vehicle. *IEEE J. Solid-State Circuits* **2017**, *52* (9), 2374–2387.
(60) Campanella, D. *Optimization of Ceramic Materials for Application as Solid-State Electrolytes in Lithium Batteries*. Doctoral Dissertation, Université du Québec à Montréal, **2023**.
(61) Gogia, A. *Improving the Safety and Efficiency of Next-Generation Liquid and Solid-State Lithium Batteries*; University of Dayton, **2021**.
(62) Kumar Mishra, G.; Gautam, M.; Bhawana, K.; Sah Kalwar, C.; Patro, M.; Anshu; Mitra, S. Exploring Chemical and Electrochemical Limitations in Sulfide Solid State Electrolytes: A Critical Review on Current Status and Manufacturing Scope. *Chem. Eur. J.* **2024**, *30* (71), No. e202402510.
(63) Liu, H.; Liang, Y.; Wang, C.; Li, D.; Yan, X.; Nan, C.; Fan, L. Priority and Prospect of Sulfide-based Solid-electrolyte Membrane. *Adv. Mater.* **2023**, *35* (50), No. 2206013.
(64) Lobe, S.; Dellen, C.; Finsterbusch, M.; Gehrke, H. G.; Sebold, D.; Tsai, C. L.; Uhlenbruck, S.; Guillon, O. Radio Frequency Magnetron Sputtering of $Li_7La_3Zr_2O_{12}$ Thin Films for Solid-State Batteries. *J. Power Sources* **2016**, *307*, 684–689.
(65) Mousavi, T.; Slattery, I.; Jagger, B.; Liu, J.; Speller, S.; Grovenor, C. Development of Sputtered Nitrogen-Doped $Li_{1+x}Al_xGe_{2-x}(PO_4)_3$

https://doi.org/10.1021/acsaelm.6c00171
ACS Appl. Electron. Mater. 2026, 8, 4855–4875

Thin Films for Solid State Batteries. *Solid State Ion.* **2021**, *364*, No. 115613.
(66) Park, J.-S.; Kim, J.-H.; Kim, H.-S. Evaluation of Electrochemical Properties of Amorphous LLZO Solid Electrolyte Through Li_2O Co-Sputtering. *Korean J. Mater. Res.* **2021**, *31* (11), 614–618.
(67) Ma, C. Y.; Briois, P.; Böhlmark, J.; Lapostolle, F.; Billard, A. $La_{9.33}Si_6O_{26}$ Electrolyte Thin Films for IT-SOFC Application Deposited by a HIPIMS/DC Hybrid Magnetron Sputtering Process. *Ionics (Kiel)*. **2008**, *14* (6), 471–476.
(68) Keraudy, J.; Athouël, L.; Hamon, J.; Girault, B.; Gloaguen, D.; Richard-Plouet, M.; Jouan, P. Y. Electrochemical Characteristics of NixN Thin Films Deposited by DC and HiPIMS Reactive Magnetron Sputtering. *Thin Solid Films* **2019**, *669*, 659–664.
(69) Sun, Z.; Liu, L.; Yang, B.; Li, Q.; Wu, B.; Zhao, J.; Ma, L.; Liu, Y.; An, H. Preparation and Ion Conduction of $Li_{1.5}Al_{0.5}Ge_{15}(PO_4)_3$ Solid Electrolyte Films Using Radio Frequency Sputtering. *Solid State Ionics* **2020**, *346*, No. 115224.
(70) Na, D.; Lee, B.; Yoon, B.; Seo, I. A Solid-State Thin-Film Electrolyte, Lithium Silicon Oxynitride, Deposited by Using RF Sputtering for Thin-Film Batteries. *J. Korean Phys. Soc.* **2020**, *76* (9), 855–859.
(71) Negishi, A.; Nozaki, K.; Ozawa, T. Thin-Film Technology for Solid Electrolyte Fuel Cells by the RF Sputtering Technique. *Solid State Ion.* **1981**, *3–4* (C), 443–446.
(72) Tajima, K.; Yamada, Y.; Bao, S.; Okada, M.; Yoshimura, K. Solid Electrolyte of Tantalum Oxide Thin Film Deposited by Reactive DC and RF Magnetron Sputtering for All-Solid-State Switchable Mirror Glass. *Sol. Energy Mater. Sol. Cells* **2008**, *92* (2), 120–125.
(73) Srivastava, P. K.; Quach, T.; Duan, Y. Y.; Donelson, R.; Jiang, S. P.; Ciacchi, F. T.; Badwal, S. P. S. Electrode Supported Solid Oxide Fuel Cells: Electrolyte Films Prepared by DC Magnetron Sputtering. *Solid State Ion.* **1997**, *99* (3–4), 311–319.
(74) Put, B.; Vereecken, P. M.; Meersschaut, J.; Sepúlveda, A.; Stesmans, A. Electrical Characterization of Ultrathin RF-Sputtered LiPON Layers for Nanoscale Batteries. *ACS Appl. Mater. Interfaces.* **2016**, *8* (11), 7060–7069.
(75) West, W. C.; Hood, Z. D.; Adhikari, S. P.; Liang, C.; Lachgar, A.; Motoyama, M.; Iriyama, Y. Reduction of Charge-Transfer Resistance at the Solid Electrolyte−Electrode Interface by Pulsed Laser Deposition of Films from a Crystalline Li_2PO_2N Source. *J. Power Sources* **2016**, *312*, 116–122.
(76) Reinacher, J.; Berendts, S.; Janek, J. Preparation and Electrical Properties of Garnet-Type $Li_6BaLa_2Ta_2O_{12}$ Lithium Solid Electrolyte Thin Films Prepared by Pulsed Laser Deposition. *Solid State Ion.* **2014**, *258*, 1–7.
(77) Ohta, N.; Takada, K.; Osada, M.; Zhang, L.; Sasaki, T.; Watanabe, M. Solid Electrolyte, Thio-LISICON, Thin Film Prepared by Pulsed Laser Deposition. *J. Power Sources* **2005**, *146* (1–2), 707–710.
(78) Indrizzi, L.; Ohannessian, N.; Pergolesi, D.; Lippert, T.; Gilardi, E. Pulsed Laser Deposition as a Tool for the Development of All Solid-state Microbatteries. *Helv. Chim. Acta* **2021**, *104* (2), No. e2000203.
(79) Zamperlin, N.; Cid, R.; Kekkonen, V.; Pesce, A.; Cheddadi, M.; Gomes, B. M.; Baptista, M. C.; Braga, M. H.; Orue, A.; López-Aranguren, P. Advanced Manufacturing of Thin-Film Lithium Metal Anode by Pulsed-Laser Deposition for next-Generation Solid-State Batteries. *J. Power Sources* **2025**, *655*, No. 237986.
(80) Tang, M.; Niu, Y.; Muhammad, W.; Muhammad, S.; Zhong, Z.; Muhammad, S.; Pang, Y.; Wan, Z.; Chen, N.; Qiao, L. Advances in Solid Oxide Fuel Cell Electrolyte Fabrication by Pulsed Laser Deposition. *Int. J. Hydrogen Energy* **2024**, *50*, 618–632.
(81) Agostinelli, J. A.; Braunstein, G. H.; Blanton, T. N. Epitaxial $LiTaO_3$ Thin Films by Pulsed Laser Deposition. *Appl. Phys. Lett.* **1993**, *63* (2), 123–125.
(82) Sakuda, A.; Hayashi, A.; Ohtomo, T.; Hama, S.; Tatsumisago, M. All-Solid-State Lithium Secondary Batteries Using $LiCoO_2$ Particles with Pulsed Laser Deposition Coatings of Li_2S-P_2S_5 Solid Electrolytes. *J. Power Sources* **2011**, *196*, 6735–6741.
(83) Kuwata, N.; Iwagami, N.; Kawamura, J. ArF Excimer Laser Deposition of Wide-Band Gap Solid Electrolytes for Thin Film Batteries. *Solid State Ionics* **2009**, *180* (6–8), 644–648.
(84) Nakagawa, A.; Kuwata, N.; Matsuda, Y.; Kawamura, J. Thin Film Lithium Battery Using Stable Solid Electrolyte Li_4SiO_4 Fabricated by PLD. *ECS Trans.* **2010**, *25* (36), 155.
(85) Kawamura, J.; Kuwata, N.; Toribami, K.; Sata, N.; Kamishima, O.; Hattori, T. Preparation of Amorphous Lithium Ion Conductor Thin Films by Pulsed Laser Deposition. *Solid State Ionics* **2004**, *175* (1–4), 273–276.
(86) Matsuda, Y.; Kuwata, N.; Kawamura, J. Thin-Film Lithium Batteries with 0.3−30 Mm Thick $LiCoO_2$ Films Fabricated by High-Rate Pulsed Laser Deposition. *Solid State Ion.* **2018**, *320*, 38–44.
(87) Kuwata, N.; Kawamura, J.; Toribami, K.; Hattori, T.; Sata, N. Thin-Film Lithium Ion Batteries with Li-V-Si-O Amorphous Solid Electrolyte Fabricated by Pulsed Laser Deposition. In *Solid State Ionics: The Science and Technology of Ions in Motion*; World Scientific, **2004**; pp 637−644.
(88) Fujimoto, D.; Kuwata, N.; Matsuda, Y.; Kawamura, J.; Kang, F. Fabrication of Solid-State Thin-Film Batteries Using $LiMnPO_4$ Thin Films Deposited by Pulsed Laser Deposition. *Thin Solid Films* **2015**, *579*, 81–88.
(89) Kuwata, N.; Kumar, R.; Toribami, K.; Suzuki, T.; Hattori, T.; Kawamura, J. Thin Film Lithium Ion Batteries Prepared Only by Pulsed Laser Deposition. *Solid State Ion.* **2006**, *177* (26–32), 2827–2832.
(90) Ito, Y.; Sakuda, A.; Ohtomo, T.; Hayashi, A.; Tatsumisago, M. Preparation of Li_2S−GeS_2 Solid Electrolyte Thin Films Using Pulsed Laser Deposition. *Solid State Ionics* **2013**, *236*, 1–4.
(91) Kazyak, E.; Chen, K.-H.; Davis, A. L.; Yu, S.; Sanchez, A. J.; Lasso, J.; Bielinski, A. R.; Thompson, T.; Sakamoto, J.; Siegel, D. J. Atomic Layer Deposition and First Principles Modeling of Glassy Li_3BO_3−Li_2CO_3 Electrolytes for Solid-State Li Metal Batteries. *J. Mater. Chem. A* **2018**, *6* (40), 19425–19437.
(92) Maximov, M. Y.; Nazarov, D.; Koshtyal, Y.; Mitrofanov, I. l.; Popovich, A. Atomic Layer Deposition of Li−Me−O Thin Films as Electrode Materials for Nanodevices Power Sources. *Proceedings* **2018**, *3*, 9.
(93) Miikkulainen, V.; Nilsen, O.; Li, H.; King, S. W.; Laitinen, M.; Sajavaara, T.; Fjellvåg, H. Atomic Layer Deposited Lithium Aluminum Oxide:(In) Dependency of Film Properties from Pulsing Sequence. *J. Vac. Sci. Technol. A* **2015**, *33* (1), No. 01A101.
(94) Chen, L.; Connell, J. G.; Nie, A.; Huang, Z.; Zavadil, K. R.; Klavetter, K. C.; Yuan, Y.; Sharifi-Asl, S.; Shahbazian-Yassar, R.; Libera, J. A. Lithium Metal Protected by Atomic Layer Deposition Metal Oxide for High Performance Anodes. *J. Mater. Chem. A* **2017**, *5* (24), 12297–12309.
(95) Luo, X.; Fiedler, A.; Azmi, R.; Xu, W.; Huang, R.; Geßwein, H.; Maibach, J.; Bruns, M.; Indris, S.; Ehrenberg, H.; Kong, X. Y. Enhancement of Ionic Conductivity in Novel LiON-AlOx Multilayer Heterostructures Prepared by Atomic Layer Deposition. *Solid State Ionics* **2021**, *373*, No. 115796.
(96) Kozen, A. C.; Pearse, A. J.; Lin, C.-F.; Noked, M.; Rubloff, G. W. Atomic Layer Deposition of the Solid Electrolyte LiPON. *Chem. Mater.* **2015**, *27* (15), 5324–5331.
(97) Heikkinen, M. *Conformality of ALD/MLD Thin Films for Microbatteries*. Master's Thesis, Aalto University, **2023**.
(98) Henderick, L.; Hamed, H.; Hamed, H.; Mattelaer, F.; Minjauw, M.; Meersschaut, J.; Dendooven, J.; Safari, M.; Safari, M.; Safari, M.; Vereecken, P.; Detavernier, C. Atomic Layer Deposition of Nitrogen-Doped Al Phosphate Coatings for Li-Ion Battery Applications. *ACS Appl. Mater. Interfaces* **2020**, *12* (23), 25949–25960.
(99) Henderick, L.; Hamed, H.; Mattelaer, F.; Minjauw, M.; Nisula, M.; Meersschaut, J.; Dendooven, J.; Safari, M.; Vereecken, P.; Detavernier, C. Plasma Enhanced Atomic Layer Deposition of a (Nitrogen Doped) Ti Phosphate Coating for Improved Energy Storage in Li-Ion Batteries. *J. Power Sources* **2021**, *497*, No. 229866.
(100) Curcio, M.; Brutti, S.; Celeste, A.; Galasso, A.; De Bonis, A.; Teghil, R. Influence of Deposition Conditions and Thermal

https://doi.org/10.1021/acsaelm.6c00171
ACS Appl. Electron. Mater. 2026, 8, 4855−4875

Treatments on Morphological and Chemical Characteristics of $Li_{6.75}La_3Zr_{1.75}Ta_{0.25}O_{12}$ Thin Films Deposited by Nanosecond PLD. *Coatings* **2023**, *13* (9), 1496.
(101) Chen, J. *Advancements in Solid-State Batteries: Pulsed Laser Deposition of Thin Film Electrolytes*. Ph.D Thesis, Technical University of Denmark, **2024**.
(102) Rawlence, M.; Garbayo, I.; Buecheler, S.; Rupp, J. L. M. On the Chemical Stability of Post-Lithiated Garnet Al-Stabilized $Li_7La_3Zr_2O_{12}$ Solid State Electrolyte Thin Films. *Nanoscale* **2016**, *8* (31), 14746–14753.
(103) Saccoccio, M.; Yu, J.; Lu, Z.; Kwok, S. C. T.; Wang, J.; Yeung, K. K.; Yuen, M. M. F.; Ciucci, F. Low Temperature Pulsed Laser Deposition of Garnet $Li_{6.4}La_3Zr_{1.4}Ta_{0.6}O_{12}$ Films as All Solid-State Lithium Battery Electrolytes. *J. Power Sources* **2017**, *365*, 43–52.
(104) Thuis, M.; Haile, S. M. Using Pulsed Laser Deposition and Microelectrodes and to Understand Ion Conductivity in Compositionally Graded Na-Ion Electrolyte (NASICON-Type) Thin Films. In *Electrochemical Society Meeting Abstracts 248*; The Electrochemical Society, Inc., **2025**; p 814.
(105) Meunier, M.; Izquierdo, R.; Hasnaoui, L.; Quenneville, E.; Ivanov, D.; Girard, F.; Morin, F.; Yelon, A.; Paleologou, M. Pulsed Laser Deposition of Superionic Ceramic Thin Films: Deposition and Applications in Electrochemistry. *Appl. Surf. Sci.* **1998**, *127*, 466–470.
(106) Izquierdo, R.; Hanus, F.; Lang, T.; Ivanov, D.; Meunier, M.; Laude, L.; Currie, J. F.; Yelon, A. Pulsed Laser Deposition of Nasicon Thin Films. *Appl. Surf. Sci.* **1996**, *96*, 855–858.
(107) Jouybari, Y. H.; Berkemeier, F.; Schäfer, A.; Schmitz, G. The Influence of Sputter Conditions on the Properties of LiPON and Its Interfaces. *J. Power Sources* **2018**, *394*, 160–169.
(108) Choi, C. H.; Cho, W. I.; Cho, B. W.; Kim, H. S.; Yoon, Y. S.; Tak, Y. S. Radio-Frequency Magnetron Sputtering Power Effect on the Ionic Conductivities of LiPON Films. *Electrochem. Solid-State Lett.* **2001**, *5* (1), A14.
(109) Mousavi, T.; Chen, X.; Doerrer, C.; Jagger, B.; Speller, S. C.; Grovenor, C. R. M. Fabrication of $Li_{1+x}Al_xGe_{2-x}(PO_4)_3$ Thin Films by Sputtering for Solid Electrolytes. *Solid State Ionics* **2020**, *354*, No. 115397.
(110) Hao, X.; Zhao, Q.; Su, S.; Zhang, S.; Ma, J.; Shen, L.; Yu, Q.; Zhao, L.; Liu, Y.; Kang, F. Constructing Multifunctional Interphase between $Li_{1.4}Al_{0.4}Ti_{16}(PO_4)_3$ and Li Metal by Magnetron Sputtering for Highly Stable Solid-state Lithium Metal Batteries. *Adv. Energy Mater.* **2019**, *9* (34), No. 1901604.
(111) Siller, V.; Morata, A.; Eroles, M. N.; Arenal, R.; Gonzalez-Rosillo, J. C.; del Amo, J. M. L.; Tarancón, A. High Performance LATP Thin Film Electrolytes for All-Solid-State Microbattery Applications. *J. Mater. Chem. A* **2021**, *9* (33), 17760–17769.
(112) Kunshina, G. B.; Bocharova, I. V.; Ivanenko, V. I. Formation of Ceramic Targets for Solid Electrolytes Sputtering. *J. Phys.: Conf. Ser.* **2021**, *1942*, 12002.
(113) Kalita, D. J.; Lee, S. H.; Lee, K. S.; Ko, D. H.; Yoon, Y. S. Ionic Conductivity Properties of Amorphous Li−La−Zr−O Solid Electrolyte for Thin Film Batteries. *Solid State Ionics* **2012**, *229*, 14–19.
(114) Koresh, I. *Li-La-Zr-O Electrolytes for All-Solid-State Li-Ion Batteries by Solution/Suspension Plasma Spray*. Doctoral dissertation, University of British Columbia, **2022**.
(115) Izumi, M.; Sasahara, N. Effect of Pre-Sintering of Raw Material Powder on Properties of Solid Oxide Fuel Cell Electrolyte Prepared by Dip-Coating Method. *J. Ceram. Soc. Japan* **2010**, *118* (1382), 944–947.
(116) Oudenhoven, J. F. M. *Deposition and Characterization of Thin Films for 3D Lithium-Ion Micro-Batteries*. Ph.D Thesis, Technische Universiteit Eindhoven, **2011**.
(117) Wu, T. T.; Guo, S.; Li, B.; Li, J. Y.; Zhang, H. S.; Ma, P. Z.; Zhang, X.; Shen, C. Y.; Liu, X. H.; Cao, A. M. Facile Construction of Nanofilms from a Dip-Coating Process to Enable High-Performance Solid-State Batteries. *ACS Appl. Mater. Interfaces* **2022**, *14* (28), 32026–32034.
(118) Gopal, V.; Clovis, K.; Björklund, S.; Balapure, A.; Goel, S.; Hall, A.; Younesi, R.; Joshi, S. Exploring Atmospheric Plasma Spraying as a Pathway to Fabricate Solid-State Battery Constituents. *Surf. Coat. Technol.* **2025**, *502*, No. 131945.
(119) Toporski, A. *Application of Cold Spray to Manufacturing of Solid-State Batteries*. MS Thesis, Rensselaer Polytechnic Institute, **2025**.
(120) Quinonez, C.; Vallejo, W.; Gordillo, G. Structural, Optical and Electrochemical Properties of TiO_2 Thin Films Grown by APCVD Method. *Appl. Surf. Sci.* **2010**, *256* (13), 4065–4071.
(121) Konar, R.; Nessim, G. D. A Mini-Review Focusing on Ambient-Pressure Chemical Vapor Deposition (AP-CVD) Based Synthesis of Layered Transition Metal Selenides for Energy Storage Applications. *Mater. Adv.* **2022**, *3* (11), 4471–4488.
(122) Floraki, C.; Sapountzis, A.; Vernardou, D. APCVD Graphene-Based Composite Electrodes for Li-Ion Batteries. *Energies* **2022**, *15* (3), No. 926.
(123) Drosos, C.; Vernardou, D. Perspectives of Energy Materials Grown by APCVD. *Sol. Energy Mater. Sol. Cells* **2015**, *140*, 1–8.
(124) Oudenhoven, J. F. M.; Van Dongen, T.; Niessen, R. A. H.; De Croon, M.; Notten, P. H. L. Low-Pressure Chemical Vapor Deposition of $LiCoO_2$ Thin Films: A Systematic Investigation of the Deposition Parameters. *J. Electrochem. Soc.* **2009**, *156* (5), D169.
(125) Jung, H.; Park, M.; Han, S. H.; Lim, H.; Joo, S.-K. Amorphous Silicon Thin-Film Negative Electrode Prepared by Low Pressure Chemical Vapor Deposition for Lithium-Ion Batteries. *Solid State Commun.* **2003**, *125* (7−8), 387–390.
(126) Chen, C.; Eichel, R.-A.; Notten, P. H. L. Metal-Organic Chemical Vapor Deposition Enabling All-Solid-State Li-Ion Microbatteries: A Short Review. *J. Electroceram.* **2017**, *38* (2), 230–247.
(127) Morosanu, C. E. *Thin Films by Chemical Vapour Deposition*; Elsevier, **1990**; Vol. 7.
(128) Xie, J.; Oudenhoven, J. F. M.; Harks, P.-P. R. M. L.; Li, D.; Notten, P. H. L. Chemical Vapor Deposition of Lithium Phosphate Thin-Films for 3D All-Solid-State Li-Ion Batteries. *J. Electrochem. Soc.* **2015**, *162* (3), A249–A254.
(129) Kim, E.; Tovar, A. G.; Ramos, E. P.; Roehling, J. D.; Hoover, S. M.; Surghani, N. E.; Radousky, H. B.; Curtis, J. S.; Ye, J.; Baker, A. A. Cold-Sprayed NMC622 Composite as a Cathode for Lithium-Ion Batteries. *ACS Appl. Mater. Interfaces* **2025**, *17*, 67152.
(130) Kim, E.; Tovar, A.; Ramos Guzman, E.; Roehling, J.; Hoover, S.; Surghani, N.; Radousky, H.; Curtis, J.; Ye, J.; Baker, A. *Cold Sprayed NMC622 Composite as Cathode for Li-Ion Batteries*; Lawrence Livermore National Laboratory (LLNL): Livermore, CA (United States), **2025**.
(131) Zhao, S.; Fu, Z.; Qin, Q. A Solid-State Electrolyte Lithium Phosphorus Oxynitride Film Prepared by Pulsed Laser Deposition. *Thin Solid Films* **2002**, *415* (1−2), 108–113.
(132) Malaki, M.; Pokle, A.; Otto, S.-K. K.; Henss, A.; Beaupain, J. P.; Beyer, A.; Müller, J.; Butz, B.; Wätzig, K.; Kusnezoff, M.; Müller, J.; Butz, B.; Wätzig, K.; Kusnezoff, M.; Janek, J.; Volz, K. Advanced Analytical Characterization of Interface Degradation in Ni-Rich NCM Cathode Co-Sintered with LATP Solid Electrolyte. *ACS Appl. Energy Mater.* **2022**, *5* (4), 4651–4663.
(133) Kuwata, N.; Lu, X.; Miyazaki, T.; Iwai, Y.; Tanabe, T.; Kawamura, J. Lithium Diffusion Coefficient in Amorphous Lithium Phosphate Thin Films Measured by Secondary Ion Mass Spectroscopy with Isotope Exchange Methods. *Solid State Ionics* **2016**, *294*, 59–66.
(134) Kuwata, N.; Iwagami, N.; Matsuda, Y.; Tanji, Y.; Kawamura, J. Thin Film Batteries with Li_3PO_4 Solid Electrolyte Fabricated by Pulsed Laser Deposition. *ECS Trans.* **2009**, *16* (26), 53.
(135) Kuwata, N.; Kawamura, J.; Toribami, K.; Hattori, T.; Sata, N. Thin-Film Lithium-Ion Battery with Amorphous Solid Electrolyte Fabricated by Pulsed Laser Deposition. *Electrochem. Commun.* **2004**, *6* (4), 417–421.
(136) Hayashi, T.; Miyazaki, T.; Matsuda, Y.; Kuwata, N.; Saruwatari, M.; Furuichi, Y.; Kurihara, K.; Kuzuo, R.; Kawamura, J. Effect of Lithium-Ion Diffusibility on Interfacial Resistance of $LiCoO_2$ Thin

https://doi.org/10.1021/acsaelm.6c00171
ACS Appl. Electron. Mater. 2026, 8, 4855−4875

Film Electrode Modified with Lithium Tungsten Oxides. *J. Power Sources* **2016**, *305*, 46–53.
(137) Shiraki, S.; Shirasawa, T.; Suzuki, T.; Kawasoko, H.; Shimizu, R.; Hitosugi, T. Atomically Well-Ordered Structure at Solid Electrolyte and Electrode Interface Reduces the Interfacial Resistance. *ACS Appl. Mater. Interfaces.* **2018**, *10* (48), 41732–41737.
(138) Wang, K.; Nishio, K.; Horiba, K.; Kitamura, M.; Edamura, K.; Imazeki, D.; Nakayama, R.; Shimizu, R.; Kumigashira, H.; Hitosugi, T. Synthesis of High-Entropy Layered Oxide Epitaxial Thin Films: $LiCr_{1/6}Mn_{1/6}Fe_{1/6}Co_{1/6}Ni_{1/6}Cu_{1/6}O_2$. *Cryst. Growth Des.* **2022**, *22* (2), 1116–1122.
(139) Sakurai, Y.; Sakuda, A.; Hayashi, A.; Tatsumisago, M. Preparation of Amorphous Li_4SiO_4–Li_3PO_4 Thin Films by Pulsed Laser Deposition for All-Solid-State Lithium Secondary Batteries. *Solid State Ionics* **2011**, *182* (1), 59–63.
(140) Ahn, J. K.; Yoon, S. G. Characteristics of Amorphous Lithium Lanthanum Titanate Electrolyte Thin Films Grown by PLD for Use in Rechargeable Lithium Microbatteries. *Electrochem. Solid-State Lett.* **2005**, *8* (2), No. A75.
(141) Brummel, I. A.; Zhou, C.; Ihlefeld, J. F. Effect of Background Gas Composition on the Stoichiometry and Lithium Ion Conductivity of Pulse Laser Deposited Epitaxial Lithium Lanthanum Tantalate ($Li_{3x}La_{1/3-x}TaO_3$). *J. Vac. Sci. Technol. A* **2024**, *42* (3), No. 032705.
(142) Furusawa, S.; Kamiyama, A.; Tsurui, T. Fabrication and Ionic Conductivity of Amorphous Lithium Meta-Silicate Thin Film. *Solid State Ion.* **2008**, *179* (15−16), 536–542.
(143) Shin-ichi, F.; Satoshi, S.; Kaduhiro, S.; Hitoshi, T. Preparation and Ionic Conductivity of β-$LiAlSiO_4$ Thin Film. *Solid State Ion.* **2004**, *167* (3), 325–329.
(144) Furusawa, S.; Tabuchi, H.; Tsurui, T. Ionic Conductivity of Lithium Alumino-Silicate Thin Films on SiO_2 Glass and Al_2O_3 Substrates. *Solid State Ionics* **2007**, *178* (15−18), 1033–1038.
(145) Sakuda, A.; Hayashi, A.; Hama, S.; Tatsumisago, M. Preparation of Highly Lithium-Ion Conductive $80Li_2S\cdot 20P_2S_5$ Thin-Film Electrolytes Using Pulsed Laser Deposition. *J. Am. Ceram. Soc.* **2010**, *93* (3), 765–768.
(146) Kim, S.; Hirayama, M.; Taminato, S.; Kanno, R. Epitaxial Growth and Lithium Ion Conductivity of Lithium-Oxide Garnet for an All Solid-State Battery Electrolyte. *Dalt. Trans.* **2013**, *42* (36), 13112–13117.
(147) Tan, J.; Tiwari, A. Characterization of $Li_7La_3Zr_2O_{12}$ Thin Films Prepared by Pulsed Laser Deposition. *Mater. Res. Soc. Symp. Proc.* **2012**, *1471* (1), 37–42.
(148) Chen, J.; Palliotto, A.; Yun, S.; Christensen, D. V.; Esposito, V.; Pryds, N. Post-Lithiation: A Way to Control the Ionic Conductivity of Solid-State Thin Film Electrolyte. *Mater. Adv.* **2023**, *4* (24), 6638–6644.
(149) Tan, J.; Tiwari, A. Fabrication and Characterization of $Li_7La_3Zr_2O_{12}$ Thin Films for Lithium Ion Battery. *ECS Solid State Lett.* **2012**, *1* (6), Q57.
(150) Morozov, A. V.; Paik, H.; Boev, A. O.; Aksyonov, D. A.; Lipovskikh, S. A.; Stevenson, K. J.; Rupp, J. L. M.; Abakumov, A. M. Thermodynamics as a Driving Factor of $LiCoO_2$ Grain Growth on Nanocrystalline Ta-LLZO Thin Films for All-Solid-State Batteries. *ACS Appl. Mater. Interfaces.* **2022**, *14* (35), 39907–39916.
(151) Lovett, A. J.; Kursumovic, A.; Dutton, S.; Qi, Z.; He, Z.; Wang, H.; MacManus-Driscoll, J. L. Lithium-Based Vertically Aligned Nanocomposite Films Incorporating $Li_xLa_{0.32}(Nb_{0.7}Ti_{0.32})O_3$ Electrolyte with High Li+ Ion Conductivity. *APL Mater.* **2022**, *10* (5), No. 051102.
(152) Sasahara, Y.; Hirose, T.; Yoshimoto, M.; Matsui, N.; Kobayashi, S.; Ubukata, H.; Takeiri, F.; Suzuki, K.; Hirayama, M.; Nishio, K.; Shimizu, R.; Kanno, R.; Kobayashi, G.; Hitosugi, T. High H− Conductivities along the Ab-Planes of La_2LiHO_3 Epitaxial Thin Films. *Cryst. Growth Des.* **2023**, *23* (10), 7103–7108.
(153) Gilardi, E.; Materzanini, G.; Kahle, L.; Döbeli, M.; Lacey, S.; Cheng, X.; Marzari, N.; Pergolesi, D.; Hintennach, A.; Lippert, T. $Li_{4-x}Ge_{1-x}P_xO_4$, a Potential Solid-State Electrolyte for All-Oxide Microbatteries. *ACS Appl. Energy Mater.* **2020**, *3* (10), 9910–9917.
(154) Montazerian, M.; Stephens, K. J.; Roddatis, V.; Vockenhuber, C.; Müller, A.; Barlow, A. J.; Lippert, T.; Shepelin, N. A.; Pergolesi, D. Enabling High-Temperature Processing of Thin Film Li-Ion Batteries Using a LISICON Based Solid-State Electrolyte. *J. Mater. Chem. A* **2026**, *14* (5), 2989–2997.
(155) Nakagawa, A.; Kuwata, N.; Matsuda, Y.; Kawamura, J. Characterization of Stable Solid Electrolyte Lithium Silicate for Thin Film Lithium Battery. *J. Phys. Soc. Jpn.* **2010**, *79* (Suppl. A), 98–101.
(156) Furusawa, S.; Kasahara, T.; Kamiyama, A. Fabrication and Ionic Conductivity of Li_2SiO_3 Thin Film. *Solid State Ionics* **2009**, *180* (6), 649–653.
(157) Furusawa, S.; Shimizu, K.; Tsurui, T. Ionic Conductivity of Li_2SiO_3 Thin Film on Sapphire Substrate. *J. Phys. Soc. Japan* **2010**, *79* (Suppl. A), 76–79.
(158) Shibata, Y.; Kaya, K.; Akashi, K.; Kanai, M.; Kawai, T.; Kawai, S. Epitaxial Growth and Surface-Acoustic-Wave Properties of $LiTaO_3$ Films Grown by Pulsed Laser Deposition. *Appl. Phys. Lett.* **1993**, *62* (23), 3046–3048.
(159) Zhang, Y.; Zheng, Z.; Liu, X.; Chi, M.; Wang, Y. Fundamental Relationship of Microstructure and Ionic Conductivity of Amorphous LLTO as Solid Electrolyte Material. *J. Electrochem. Soc.* **2019**, *166* (4), A515.
(160) Xia, H.; Wang, H. L.; Xiao, W.; Lai, M. O.; Lu, L. Thin Film Li Electrolytes for All-Solid-State Micro-Batteries. *Int. J. Surf. Sci. Eng.* **2009**, *3* (1−2), 23–43.
(161) Ke, B.; Wang, X. Integratable All-Solid-State Thin-Film Microbatteries. *Proc. Natl. Acad. Sci. U. S. A.* **2025**, *122* (16), No. e2415693122.
(162) Wang, C.; Wang, C.; Li, M.; Zhang, S.; Zhang, C.; Chou, S.; Mao, J.; Guo, Z. Design of Thin Solid-State Electrolyte Films for Safe and Energy-Dense Batteries. *Mater. Today* **2024**, *72*, 235–254.
(163) Atwal, S.; Bhasin, V.; Nayak, C.; Nagendra, A.; Karki, V.; Sahoo, P. K.; Bhattacharyya, K.; Bhattacharyya, D.; Biswas, A. Spectroscopic Ellipsometry Study of TiO_2/LiPON and LNMC/LiPON Solid Electrode/Electrolyte Interfaces of Solid-State Batteries. *ACS Appl. Energy Mater.* **2025**, *8* (11), 7730–7743.
(164) Yuwono, J. A.; Burr, P.; Galvin, C.; Lennon, A. Atomistic Insights into Lithium Storage Mechanisms in Anatase, Rutile, and Amorphous TiO_2 Electrodes. *ACS Appl. Mater. Interfaces.* **2021**, *13* (1), 1791–1806.
(165) Uddin, M.-J.; Letfullina, A. R.; Alaboina, P. K.; Cho, J.-S.; Cho, S.-J. Synthesis of Nanoscale $Li_7La_3Zr_2O_{12}$ Solid State Electrolyte By Spray Drying. *ECS Meet. Abstr.* **2017**, *MA2017-02* (52), 2150.
(166) Ahn, J. K.; Yoon, S. G. Characteristics of Perovskite $Li_{0.5}La_{0.5}TiO_3$ Solid Electrolyte Thin Films Grown by Pulsed Laser Deposition for Rechargeable Lithium Microbattery. *Electrochim. Acta* **2004**, *50* (2-3), 371–374.
(167) Ahn, J.-K.; Yoon, S.-G.; Kim, C. S. Effect of $Li_{0.5}La_{0.5}TiO_3$ Solid Electrolyte Films on Electrochemical Properties of $LiCoO_2$ Thin Film Cathodes with Different Rapid-Thermal Annealing Conditions. *J. Vac. Sci. Technol. B* **2005**, *23* (5), 2089–2094.
(168) Kuwata, N.; Hasegawa, G.; Maeda, D.; Ishigaki, N.; Miyazaki, T.; Kawamura, J. Tracer Diffusion Coefficients of Li Ions in $Li_xMn_2O_4$ Thin Films Observed by Isotope Exchange Secondary Ion Mass Spectrometry. *J. Phys. Chem. C* **2020**, *124* (42), 22981–22992.
(169) Hasegawa, G.; Kuwata, N.; Tanaka, Y.; Miyazaki, T.; Ishigaki, N.; Takada, K.; Kawamura, J. Tracer Diffusion Coefficients of Li+ions Inc-Axis Oriented Li_xCoO_2 thin Films Measured by Secondary Ion Mass Spectrometry. *Phys. Chem. Chem. Phys.* **2021**, *23* (3), 2438–2448.
(170) Kawamura, J.; Kuwata, N.; Suzuki, T.
(171) Haruta, M.; Shiraki, S.; Ohsawa, T.; Suzuki, T.; Kumatani, A.; Takagi, Y.; Shimizu, R.; Hitosugi, T. Preparation and In-Situ Characterization of Well-Defined Solid Electrolyte/Electrode Interfaces in Thin-Film Lithium Batteries. *Solid State Ionics* **2016**, *285*, 118–121.
(172) Matsuda, Y.; Kuwata, N.; Okawa, T.; Dorai, A.; Kamishima, O.; Kawamura, J. In Situ Raman Spectroscopy of Li_xCoO_2 Cathode in Li/

https://doi.org/10.1021/acsaelm.6c00171
ACS Appl. Electron. Mater. 2026, 8, 4855−4875

$Li_3PO_4/LiCoO_2$ All-Solid-State Thin-Film Lithium Battery - ScienceDirect. *Solid State Ion.* **2019**, *335*, 7–14.
(173) Kato, M.; Hayashi, T.; Hasegawa, G.; Lu, X.; Miyazaki, T.; Matsuda, Y.; Kuwata, N.; Kurihara, K.; Kawamura, J. Electrochemical Properties of $LiCoO_2$ Thin Film Surface Modified by Lithium Tantalate and Lithium Niobate Coatings. *Solid State Ion.* **2017**, *308*, 54–60.
(174) Ishiguro, N.; Totsuka, T.; Uematsu, H.; Sekizawa, O.; Yamamoto, K.; Iriyama, Y.; Takahashi, Y. Comprehensive Operando Visualization of the Electrochemical Events in the Cathode/Anode Layers in Thin-Film-Type All-Solid-State Lithium-Ion Batteries. *ACS Appl. Energy Mater.* **2023**, *6* (15), 8306–8315.
(175) Hikima, K.; Shimizu, K.; Kiuchi, H.; Hinuma, Y.; Suzuki, K.; Hirayama, M.; Matsubara, E.; Kanno, R. Operando Analysis of Electronic Band Structure in an All-Solid-State Thin-Film Battery. *Commun. Chem.* **2022**, *5* (1), 52.
(176) Xu, Y.; Dong, K.; Kochovski, Z.; Wu, Q.; Lu, Y. Advancing Cryogenic Electron Microscopy towards Mechanistic Understanding of Metal Electrodes and Interphases *EES Batteries* **2026**.
(177) Liu, Y.; Ju, Z.; Zhang, B.; Wang, Y.; Nai, J.; Liu, T.; Tao, X. Visualizing the Sensitive Lithium with Atomic Precision: Cryogenic Electron Microscopy for Batteries. *Acc. Chem. Res.* **2021**, *54* (9), 2088–2099.
(178) Ren, X.; Zhang, X.; Xu, R.; Huang, J.; Zhang, Q. Analyzing Energy Materials by Cryogenic Electron Microscopy. *Adv. Mater.* **2020**, *32* (24), No. 1908293.
(179) Cheng, D.; Lu, B.; Raghavendran, G.; Zhang, M.; Meng, Y. S. Leveraging Cryogenic Electron Microscopy for Advancing Battery Design. *Matter* **2022**, *5* (1), 26–42.
(180) Uxa, D.; Holmes, H. J.; Meyer, K.; Dörrer, L.; Schmidt, H. Lithium Tracer Diffusion in $LiNi_{0.33}Mn_{0.33}Co_{0.33}O_2$ cathode Material for Lithium-Ion Batteries. *Phys. Chem. Chem. Phys.* **2021**, *23* (10), 5992–5998.
(181) Uxa, D.; Schmidt, H. Lithium Tracer Diffusion in near Stoichiometric $LiNi_{0.5}Mn_{15}O_4$ cathode Material for Lithium-Ion Batteries. *Z. Phys. Chem.* **2022**, *236* (6−8), 979–989.
(182) Kuwata, N.; Nakane, M.; Miyazaki, T.; Mitsuishi, K.; Kawamura, J. Lithium Diffusion Coefficient in $LiMn_2O_4$ Thin Films Measured by Secondary Ion Mass Spectrometry with Ion-Exchange Method. *Solid State Ionics* **2018**, *320*, 266–271.
(183) Hüger, E.; Schmidt, H. Lithium Tracer Diffusion in Ion-Beam Sputtered Nano-Crystalline and Amorphous $LiNi_{0.33}Mn_{0.33}Co_{0.33}O_2$ Films. *Solid State Ionics* **2024**, *417*, No. 116702.
(184) Uxa, D.; Hüger, E.; Schmidt, H. Li Diffusion in Thin-Film LiySi Electrodes: Galvanostatic Intermittent Titration Technique and Tracer Diffusion Experiments. *J. Phys. Chem. C* **2020**, *124* (51), 27894–27899.
(185) Schwab, C.; Höweling, A.; Windmüller, A.; Gonzalez-Julian, J.; Möller, S.; Binder, J R; Uhlenbruck, S.; Guillon, O.; Martin, M. Bulk and Grain Boundary Li-Diffusion in Dense $LiMn_2O_4$ Pellets by Means of Isotope Exchange and ToF-SIMS Analysis. *Phys. Chem. Chem. Phys.* **2019**, *21* (47), 26066–26076.

https://doi.org/10.1021/acsaelm.6c00171
ACS Appl. Electron. Mater. 2026, 8, 4855−4875